

Chapter 4

Nonlinear Dynamics: from Simple to Complex

We now examine in more detail the theoretical context where the convection experiments described in the previous chapter can be best situated. The interest of this study stems from the fact that most instabilities that develop in bounded continuous media enter the framework of dynamical systems theory. Its foundation rests on an analysis of the effects of lateral confinement, §4.1. In a strongly confined system, even far enough from the instability threshold, the space dependence of unstable modes remains frozen and the state of the system is sufficiently well characterized by few amplitudes playing the role of effective degrees of freedom, which permits the analysis of the transition to turbulence in the spirit of Chapter 2. Here we limit ourselves to a heuristic presentation of the recent developments of nonlinear dynamics without insisting much on mathematical aspects.

We are thus mainly interested in characterizing sustained regimes of *dissipative dynamical systems* obtained after the decay of transients. These asymptotic regimes reached in the limit $t \rightarrow \pm\infty$ are represented in phase space by objects called *limit sets*. Stable limit sets are reached in the normal course of time, *i.e.* for $t \rightarrow +\infty$ and unstable limit set in the reverse case $t \rightarrow -\infty$. We have already seen examples of limit sets, *fixed points* and *limit cycles* for time-independent and periodic regimes, respectively. More complicated, multi-periodic and chaotic, behaviors are accounted for by objects called *limit tori* and *strange attractors*, which remain to be introduced. The second main purpose of this chapter is the description of the growth of complexity observed as the number of instability modes increases when control parameters are varied. The transitions from time-independent states to regular periodic or multi-periodic regimes, next to chaos, take place according to *universal scenarios* that are independent of the particular system studied. Section 4.2 is devoted to the simplest ones.

By contrast with regular regimes, chaotic states are characterized by their *unpredictability*, generally associated with a *fractal* occupation of phase space. These different facets are introduced at a theoretical level in Section 4.3. Next we turn to *empirical* approaches useful to interpret experimental results in Section 4.4.

However, all this is valid only in so far as the projection of the dynamics onto well isolated spatially frozen modes makes sense. In practice, unfreezing takes place when lateral confinement effects are not strong enough to maintain coherence much beyond the cell size. In systems with many cells chaos then develops both in time and in space, but this topic is deferred to Chapter 5.

4.1 Reduction of the Number of Degrees of Freedom

4.1.1 Role of aspect ratios

Let us come back to eigenmodes obtained from the linear stability analysis of the instability studied, *e.g.* convection. The problem has been formalized in Section 3.1.3, p. 75. We assume that confinement is specified by *lateral* boundary conditions at a distance ℓ , whereas the instability generates cells with typical scale λ_c . The aspect ratio can be defined as $\Gamma = \ell/\lambda_c$. The difference between the cases “ $\Gamma \sim 1$ ” and “ $\Gamma \gg 1$ ” is illustrated in Figure 4.1 and 4.2. Exercises 4.6.1 and 4.6.2 should be worked out to gain a more analytical understanding of the problem.

We first consider the case when the horizontal dimensions are of the order of the wavelength λ_c so that all modes are physically distinct (Fig. 4.1). Only the value of the corresponding thresholds R_1, R_2, \dots matters, the two-dimensional presentation of the different modes is given just in order to rationalize the classification in terms of the number of substructures in x and z , which is supported by the idea that these states should stay close to the branches that would exist in the absence of lateral boundary conditions (fine solid lines). They account for a kind of spatial resonance between the lateral extension of the system and the length scale originating from the instability mechanism, ending in the formation of an integer number of roughly circular cells, as already illustrated in Figure 3.8 (top), p. 96 (visualization of convection in silicon oil). The lower branch would then correspond to the “fundamental” states with one layer of cells and the upper one to “excited” states with two layers of cells stacked one above the other as could be obtained at higher values of the control parameter.

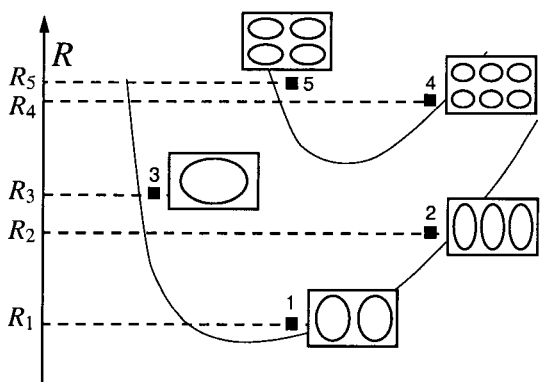


Fig. 4.1 Spectrum of the linearized stability problem for a confined system, $\Gamma \sim 1$; for $R_1 < R < R_2$, mode 1 is unstable, the others are stable.

In practice, the actual structure of the modes can be obtained at the price of a full three-dimensional calculation, in general difficult and with little supplementary insight into their physical significance. Since the spectrum of the linear stability problem is entirely made of isolated values far from one another, it is in principle easy to limit the number of linearly excited modes ($R > R_n$ hence $\sigma_n > 0$) from those that are still damped ($R < R_m$, $\sigma_m < 0$, $|\sigma_m| \gg 1$).

By contrast, when $\Gamma \gg 1$, that is $\ell \gg \lambda_c$ (Figure 4.2), the spectrum is quasi-continuous. It is obtained from the dispersion relation for a laterally unbounded system by adding a quantization condition on the wavevector, typically $k_n \sim \pi n / \ell$ for n cells of width $\lambda/2$ over a interval of width ℓ . The difference between neighboring wavevectors for patterns with ± 1 cell is $k_{n+1} - k_n = \pi / \ell \ll k_c$, which is small when ℓ is large. Close to k_c , owing to the quadratic shape of the dispersion relation (3.26), p. 84, one expects $(R_{n_c \pm 1} - R_{n_c}) / R_c = \xi_0^2 \pi^2 / \ell^2$, where n_c is here the number of cells expected at threshold and given by $n_c \lambda_c / 2 \simeq \ell$. Corresponding modes are thus quasi-degenerate. Apart from the precise value of the wavevector, all modes of the lowest branch are expected to have similar spatial structures. The interactions between modes can then be understood as interferences yielding modulated patterns, also called *textures*, as illustrated in Figure 3.10, p. 98. The present chapter is entirely devoted to the case $\Gamma \sim 1$ and to the development of *temporal chaos* phenomenologically introduced in Chapter 3, Section 3.2.3, p. 94, and is thus placed in direct continuity with Chapter 2.

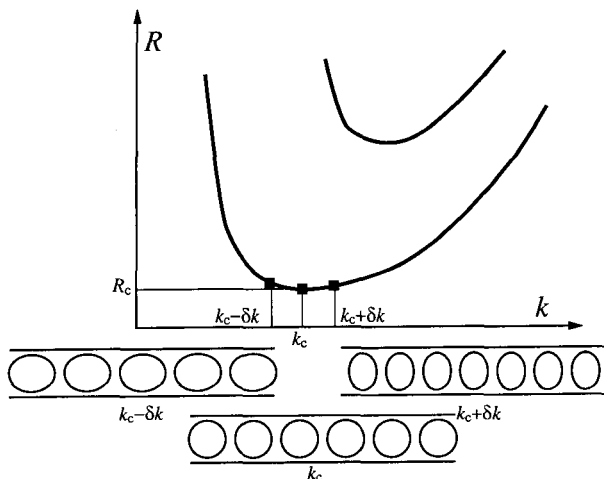


Fig. 4.2 Spectrum of the linearized stability problem for an extended system, $\Gamma \gg 1$; for $R > R_c$ the modes belonging to a range $\mathcal{O}(\sqrt{R - R_c})$ centered at k_c are unstable and may serve to build the nonlinear pattern.

4.1.2 Low dimensional effective dynamics

4.1.2.1 Framework

From a general viewpoint, it may seem reasonable to take advantage of the work done in solving the linear stability problem to treat the nonlinear problem. This is done by expanding the solution onto the basis of eigenmodes:

$$\mathbf{V} = \sum_n A_n \mathbf{X}_n, \quad (4.1)$$

and then searching the equations to be fulfilled by the amplitudes A_n of the modes \mathbf{X}_n , in order to extend the linear dynamics simply governed by $\dot{A}_n = s_n A_n$ to the nonlinear range. From the qualitative arguments developed above, we are led to think that the unstable and neutral modes play the most active role and that the stable modes more passively evolve under the forcing action of the others.

Let us incorporate this feature in the formalism itself and assume that the problem is initially posed in the general form:

$$\dot{\mathbf{V}} = \mathcal{L}\mathbf{V} + \mathcal{N}(\mathbf{V}), \quad (4.2)$$

where \mathcal{L} accounts for the linear interactions and where $\mathcal{N}(\mathbf{V})$ is at least

quadratic in \mathbf{V} . An appropriate projection of the equations onto the eigenbasis yields a dynamical system for the amplitudes A_n introduced through (4.1), which formally reads:

$$\dot{A}_n = s_n A_n + \sum_{mp} g_{n,mp} A_m A_p + \dots, \quad (4.3)$$

where the coefficient $g_{n,mp}$ describes how the interaction of modes \mathbf{X}_m and \mathbf{X}_p contributes to the dynamics of mode \mathbf{X}_n . In fact this projection procedure is rarely achievable without approximation (and further modeling of the physical situation). A favorable case is when the analytical expression of eigenmodes can be handled by hand (or using formal algebra software), for example trigonometric functions as illustrated in Exercises 4.6.1 and 4.6.2. Otherwise one can attempt to extend to the nonlinear domain the *Galerkin method* already used at the linear stage, *e.g.* in the second part of Exercise 3.3.2, p. 107.

Progress made by replacing the primitive problem expressed in terms of partial differential equations by (4.3), *i.e.* a differential system of infinite order, may seem slight. However, it is very powerful when combined with the idea of separating *driving* modes and *enslaved* modes to truncate the system, eliminate the latter and obtain an effective system involving only the former. This is the *adiabatic elimination procedure* advanced as the founding principle of *synergetics*, the science of nonlinear cooperative phenomena in out-of-equilibrium systems [Haken (1983)].

Let us consider a system on the verge of bifurcating or having just bifurcated ($R \approx R_c$). This comes to the assumption that, among all linear eigenmodes, we can isolate a small subgroup of those that are “dangerous,” nearly neutral, either unstable or stable but slightly, *i.e.* with the real parts σ of their growth rates either positive or negative but small. Strictly speaking, the *center subspace*, subscript ‘c’, is the space spanned by eigenmodes having eigenvalues with $\sigma = 0$ exactly, and we assume that we have n_c such modes. On general grounds, having n_c strictly critical modes is a problem of codimension n_c , since n_c conditions $\sigma_n(\mathbf{r}) = 0$ have to be fulfilled, \mathbf{r} being the set of control parameters. In practice, we can vary only one control parameter while remaining in the vicinity of a manifold of codimension n_c in parameter space, hence $\sigma_c \approx 0$ for n_c driving modes that by extension will continue to be labelled with the same subscript.

On the contrary, all other modes are supposed to remain *stable*, hence with subscript¹ ‘s’ and a related assumption $\sigma_s < 0$, meaning more precisely

¹So, ‘c’ may equally well mean ‘central’ or ‘critical’ and ‘s’ either ‘stable’ or ‘slave’!

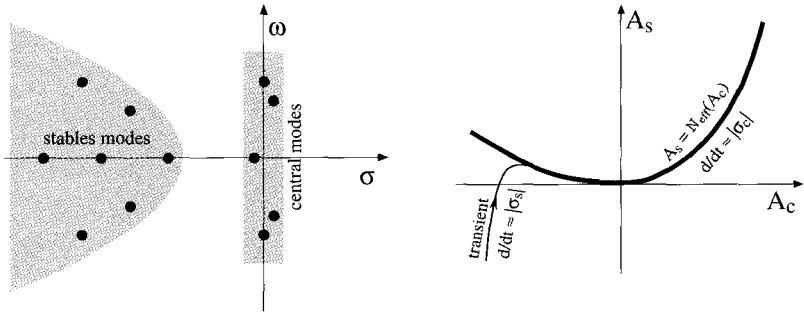


Fig. 4.3 Left: Spectrum of a linear operator with a group of *center modes* separated from *stable modes* by a wide ‘spectral gap’. Right: Adiabatic elimination of stable modes. The whole sets of center-mode and stable-mode amplitudes are featured by axes \mathbf{A}_c and \mathbf{A}_s , respectively. A trajectory starting anywhere in phase space rapidly migrates towards a *center manifold* with equation (4.6) which is the nonlinear extrapolation of the center subspace at the origin ($\mathbf{A}_s = 0$), then slowly evolves along it according to the effective dynamics (4.7).

that $|\sigma_c| \ll |\sigma_s|$, so that the driving modes have relaxation rates well separated from those of the enslaved modes. The linear spectrum is therefore supposed to display a wide *spectral gap*, see Figure 4.3 (left).

The effective dynamics is obtained by elimination of the enslaved modes. For simplicity we consider a d -dimensional case, $d < \infty$, with n_c driving modes and $n_s = d - n_c$ stable modes. The considerations developed now can be, at least at a heuristic level, easily extended to the infinite dimensional case corresponding to instabilities in continuous media, with an infinite number of stable modes and the series of eigenvalues with real parts extending down to $-\infty$. The adaptation of this elimination procedure to the case of extended systems will be sketched in Chapter 5.

4.1.2.2 Heuristic approach

Let us explicitly separate driving modes with amplitudes collectively denoted as \mathbf{A}_c from enslaved ones with amplitudes \mathbf{A}_s in (4.3). For the driving modes we get:

$$\dot{\mathbf{A}}_c = \mathcal{L}_c \mathbf{A}_c + \mathcal{N}_c(\mathbf{A}_c, \mathbf{A}_s), \quad (4.4)$$

where \mathcal{L}_c is the restriction of the linearized operator \mathcal{L}_r to the space spanned by the \mathbf{A}_c and \mathcal{N}_c accounts for the nonlinear interactions between

driving and enslaved modes. Similarly we write:

$$\dot{\mathbf{A}}_s = \mathcal{L}_s \mathbf{A}_s + \mathcal{N}_s(\mathbf{A}_c, \mathbf{A}_s) \quad (4.5)$$

for the amplitudes of stable modes. The idea of the reduction is to solve the problem for the stable modes as if they were submitted to a forcing from the (slowly evolving) driving modes, then to insert the solution back into (4.4) to obtain the effective dynamical system we are looking for.

In order to simplify the application of this strategy, let us assume that the s_s are real and non degenerate, and that \mathcal{N}_s involves only the \mathbf{A}_c so that we can rewrite (4.5) in a basis such that \mathcal{L}_s is in diagonal form, which leads to:

$$\dot{\mathbf{A}}_s + |s_s| \mathbf{A}_s = \mathcal{N}_s(\mathbf{A}_c(t)) .$$

It is easily checked that the complete solution of this non-homogeneous linear problem reads

$$\mathbf{A}_s(t) = \exp(-|s_s|t) \mathbf{A}_s(0) + \int_0^t \exp(-|s_s|(t-t')) \mathcal{N}_s(\mathbf{A}_c(t')) dt'$$

where $\mathbf{A}_s(0)$ is specified by the initial conditions at $t = 0$. According to the assumption made about the stable part of the spectrum, we see that the first term on the right hand side contributes to the solution only during a brief transient of duration $\mathcal{O}(1/|s_s|)$ and that, in the integral, the exponential kernel is short-range so that we may approximate the solution as

$$\mathbf{A}_s(t) \approx \frac{1}{|s_s|} \mathcal{N}_s(\mathbf{A}_c(t)) . \quad (4.6)$$

In the d -dimensional phase space, these $n_s = d - n_c$ relations define a n_c -dimensional manifold parameterized by the n_c amplitudes of the driving modes. Inserting them into the evolution equations for the \mathbf{A}_c , we get:

$$\dot{\mathbf{A}}_c = \mathcal{L}_c \mathbf{A}_c + \mathcal{N}_c(\mathbf{A}_c, \mathcal{N}_s(\mathbf{A}_c)) = \mathcal{L}_c \mathbf{A}_c + \mathcal{N}_{\text{eff}}(\mathbf{A}_c) , \quad (4.7)$$

which defines an *effective dynamics* on this manifold. An example is treated in Exercise 4.6.2.

4.1.3 Center manifolds and normal forms

4.1.3.1 Reduction to the center manifold

The result illustrated in Figure 4.3 (right) can be derived in a mathematically rigorous way, asymptotically valid at the long time limit, *i.e.*

$t \gg 1/\min(|\sigma_s|)$. This approach is called the *center manifold reduction*.² Assuming that, as suggested by the heuristic approach, the stable modes “live” on a slow manifold defined through

$$\mathbf{A}_s = \mathcal{H}(\mathbf{A}_c), \quad (4.8)$$

one can determine the functional equation governing \mathcal{H} by inserting (4.8) in (4.5) and replacing $\dot{\mathbf{A}}_c$ by its expression from (4.4). This yields

$$\partial \mathcal{H}(\mathbf{A}_c) \cdot \left[\mathcal{L}_c \mathbf{A}_c + \mathcal{N}_c(\mathbf{A}_c, \mathcal{H}(\mathbf{A}_c)) \right] = \mathcal{L}_s \mathcal{H}(\mathbf{A}_c) + \mathcal{N}_s(\mathbf{A}_c, \mathcal{H}(\mathbf{A}_c)),$$

where $\partial \mathcal{H}$ denotes the Jacobian matrix of \mathcal{H} with elements $\mathcal{H}_{ij} = \partial \mathcal{H}_i / \partial A_{cj}$. This functional equation for \mathcal{H} is then solved by representing $\mathcal{H}(\mathbf{A}_c)$ as a formal series in powers of the components of \mathbf{A}_c :

$$\mathcal{H}(\mathbf{A}_c) \equiv \sum_{n \geq 2} \mathcal{H}_n(\mathbf{A}_c),$$

where $\mathcal{H}_n(\mathbf{A}_c)$ is a polynomial formed with a series of homogeneous increasing-degree monomials in the form:

$$\prod_{m=1}^{d_c} A_{cm}^{n_m}, \quad n_m \geq 0, \quad \sum_m n_m = n,$$

with coefficients to be determined by identification. The so-obtained expression is further inserted in (4.4), which leads to the effective dynamics one is looking for.

4.1.3.2 Reduction to the normal form

In practice, the physical contents of the expression just obtained for the effective dynamics is obscured by the presence of a large number of terms that can be eliminated by nonlinear changes of variables, in much the same way as linear changes of variables allow one to represent a linear operator in its (much more transparent) Jordan normal form. This supplementary step, called *normal form reduction* leads to the elimination of all non-resonant terms in the effective dynamical system. The term “resonant” is here understood in the same way as in the study of the improper node, Chapter 2, p. 40, or more generally in Appendix A, §A.2, p. 334.

²See for example: J.D. Crawford, “Introduction to bifurcation theory” Rev. Mod. Phys. **63** (1991) 991–1037.

For example, let us consider the case of a two-dimensional center manifold parameterized with a pair of complex conjugate modes (Z, Z^*) with eigenvalues $\pm i\omega_c$, $\omega_c \neq 0$,³ exactly marginal at some specific value $\mathbf{r} = \mathbf{r}_c$ of the set of control parameters, i.e. $\sigma(\mathbf{r}_c) = 0$. Consider one of these variables, say Z , the previous reduction procedure generically leads to an effective dynamics

$$\dot{Z} = -i\omega_c Z + \sum_{m=0}^2 g_m^{(2)} Z^{2-m} Z^{*m} + \sum_{m=0}^3 g_m^{(3)} Z^{3-m} Z^{*m} + \dots, \quad (4.9)$$

where the coefficients $g_m^{(n)}$ are complex *a priori*. The equation governing the other variable Z^* is of course the complex conjugate of (4.9). It is however easily seen that none of the quadratic terms present in these equations is resonant:

Looking for a solution of (4.9) as an expansion in powers of Z , at first order we indeed get $Z^{(1)} \propto \exp(-i\omega_c t)$. The correction brought by the first quadratic term is then a solution to:

$$\dot{Z}^{(2)} + i\omega_c Z^{(2)} \propto (Z^{(1)})^2 \sim \exp(-2i\omega_c t),$$

that admits $\exp(-2i\omega_c t)$ as special solution with a non-singular coefficient. Terms

$$ZZ^* \sim 1 \quad \text{and} \quad (Z^*)^2 \sim \exp(2i\omega_c t)$$

are non-resonant for the same reason and, among cubic terms only the monomial

$$Z^* Z^2 = |Z|^2 Z \sim \exp(-i\omega_c t)$$

turns out to be resonant. It is just a little long and tedious to find the change of variables:

$$Z = \bar{Z} + \sum_{m=0}^2 a_m^{(2)} \bar{Z}^{2-m} (\bar{Z}^*)^m + \sum_{m=0}^3 a_m^{(3)} \bar{Z}^{3-m} (\bar{Z}^*)^m + \dots \quad (4.10)$$

that leads to the so-call *normal form*:

$$\dot{\bar{Z}} = -i\omega_c \bar{Z} + \bar{g}_3 |\bar{Z}|^2 \bar{Z} + \dots \quad (4.11)$$

appropriate to the case at hand.

³ $\omega_c \neq 0$ means $\omega_c \sim \mathcal{O}(1)$ since $\omega_c \ll 1$ would rather correspond to a reference situation with a double root $s = 0$, perturbed so as to display real and imaginary parts that would be simultaneously small.

4.1.3.3 Slightly off the critical conditions

One last step remains to be performed. Up to now we have assumed that the control parameters had precisely the values that make the relevant modes marginal. This defines a *critical surface* in parameter space, $\mathbf{r} = \mathbf{r}_c$. Close to this surface, the condition is no longer fulfilled but the real parts of the growth rates remain small.

A first-order Taylor expansion of these growth rates in a direction of the parameter space that is transverse (*i.e.* not tangent) to the critical surface allows one to get off the critical conditions. Let us simply denote the coordinate in that direction by r . For the pair of complex modes considered above, this comes to take:

$$s = \sigma \pm i\omega \quad \text{with} \quad \sigma \propto r, \quad \omega \approx \omega_c, \quad g_3 \approx \bar{g}_3,$$

and to “unfold” the critical dynamics (4.11) by correcting the growth rate, hence $-i\omega_c \mapsto s = \sigma - i\omega_c$. This corrected form⁴ will be used below to account for the emergence of periodicity. A rewarding exercise is to derive it explicitly from Equation (2.42) governing the van der Pol oscillator, p. 48.

4.1.3.4 Universality and modeling

More generally, one may remark that the normal form and the perturbations that describe the departure from criticality depend in an essential way on resonance relations existing among the eigenvalues of the linearized stability problem at criticality. In the previous example we had:

$$s_1 = s_2 + 2s_1 \quad \text{for} \quad s_{1,2} = s_{\pm} = \pm i\omega_c,$$

which renders the term Z^*Z^2 resonant. Here, the precise reason is:

$$\exp(s_2 t) \exp(s_1 t)^2 \equiv \exp[(s_2 + 2s_1)t] = \exp(s_1 t)$$

with $s_2 = i\omega_c$ and $s_1 = -i\omega_c$, but the generalization is immediate to any resonance and leads to the identification of nonlinear resonant terms.

This plain observation underlies the notion of *universality*:

All systems that bifurcate in the same way, have the same symmetries, and are controlled by the same number of parameters, have qualitatively similar dynamics.

⁴In line with the remark in Note 3, p. 123, it is assumed that $\sigma \ll \omega_c \sim \mathcal{O}(1)$ because admitting $\sigma \sim \omega_c$ is not compatible with the idea of a near-marginal situation.

To set this similarity on a quantitative footing requires complicated and tedious changes of variables that can be avoided by having recourse to *phenomenological modeling* of the considered system close to its critical conditions, that is:

- 1) Determine the linear normal form governing the driving modes, identify the corresponding resonance conditions and add the most general linear perturbations corresponding the departure from criticality (see Appendix A, §A.2, and more specifically §A.2.3).
- 2) Introduce all possible nonlinear resonant terms —different equivalent forms are admissible— with appropriate phenomenological coefficients. (Notice that these coefficients could be fitted from well-designed on-purpose experiments.)
- 3) Takes full advantage of a preliminary abstract mathematical study (with few generic parameters) to account for the behavior of the specific system considered as its control parameters are varied.

4.2 Transition to Chaos

The approach in terms of low dimensional *dynamical systems* now being established, we now briefly illustrate the theoretical approach to the growth of complexity until chaos is obtained. At steady state, a chaotic regime is characterized by an evolution that, in spite of being governed by a deterministic system, has lost its long-term predictability.

As empirically shown in Chapter 3, complex evolution is observed when the system is driven ever farther from equilibrium at the end of an instability cascade. The understanding of this cascade relies on the progressive increase of the dimension of the manifold on which the effective dynamics develops. By varying the control parameter, one increases the number of potentially unstable modes (see Figure 4.1) and thus the dimension of the effective dynamical system.

While one variable is enough to account for transitions between time-independent regimes, we need two for periodic motion, and even more for more complicated behavior, regular (multi-periodic in practice) or irregular.

4.2.1 First steps: time-independent and periodic regimes

4.2.1.1 Bifurcation between time-independent regimes

The simplest case is of course that of time-independent regimes accounted for by fixed points in phase space. Accordingly, the simplest bifurcations are also those that correspond to transitions from one time-independent regime to another. In practice, they can be accounted for by a single variable through appropriate generalizations of the Landau model (1.19), p. 13, see Exercise 4.6.3 for further relevant considerations.

Let us start with:

$$\dot{A} = rA - gA^3 + H, \quad (4.12)$$

describing the evolution of a system at a perturbed supercritical bifurcation. The dynamics described by (4.12) is typical of convection which, as we have seen, is a stationary instability that saturates beyond threshold ($r > 0$, $g > 0$). Here time t has been rescaled with the natural evolution time τ_0 of the unstable mode.

Quantity H measures the intensity of some perturbation coupled to the instability mode. In convection this could be an induction process producing a modulation of the background fluid density through non-uniform heating, which encourages the rising or sinking of the fluid already in the absence of temperature gradient. See also the remark on the facing page.

The *bifurcation diagram*,⁵ corresponding to (4.12), is displayed in Figure 4.4. The diagram corresponding to *perfect bifurcation*, with $H = 0$, features:

$$A_* = \pm(r/g)^{1/2} \quad (4.13)$$

and has already been displayed in Figure 1.4, p. 14. It is recalled here as a fine solid line. In the general case, the fixed points A_* of (4.12), obtained by solving it for A when $\dot{A} = 0$, now depend on r and H . The introduction of a small field $H \neq 0$ induces a non-trivial response $A_* \neq 0$ below the theoretical bifurcation point at $r = 0$. This response remains small as long as r is large and negative, so that

$$A_* \approx (-1/r)H, \quad (4.14)$$

but closer to the threshold, as $|r|$ decreases, the amplitude of the response

⁵The bifurcation diagram is a graph locating the fixed points, and more generally the limit sets, as functions of the control parameters.

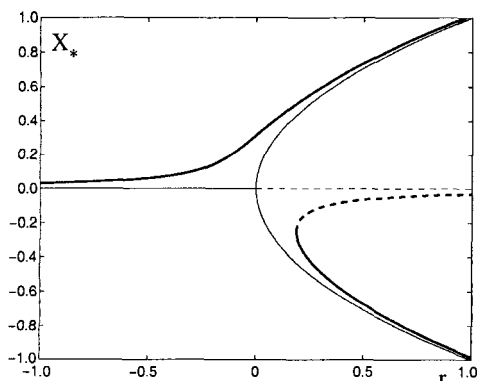


Fig. 4.4 *Imperfect* fork bifurcation accounted for by (4.12) with $g = 1$ for $H = 0.054$. Thick solid line (dashed line) corresponds to stable (unstable) fixed points as functions of r . The thin solid line is for the perfect bifurcation when $H = 0$ already displayed in Figure 1.4, p. 14.

increases up to a point where nonlinearities can no longer be neglected. For $r = 0$ this yields

$$A_* = (H/g)^{1/3}. \quad (4.15)$$

When r varies from $-\infty$ to $+\infty$, A_* follows a first branch of stable solutions, the thick line that continuously joins the axis $A = 0$ for $r \rightarrow -\infty$ to the arc of parabola $A_* = +(r/g)^{1/2}$ for $r \rightarrow +\infty$. Sufficiently above threshold ($r > 0$), a second branch appears, disconnected from the first, that joins the arc of parabola $A_* = -(r/g)^{1/2}$ in its stable part (continuous thick line) to the axis $A = 0$ for $r \rightarrow +\infty$ in its unstable part (dashed line). The singularity at $r = A = 0$ has disappeared and one speaks of an *imperfect bifurcation*. In convection, a tiny forcing by thermal impression of a given pattern would produce this effect. The detailed study of this bifurcation diagram and other related ones is the subject of Exercise 4.6.3.

Remark

This description is in fact in close correspondence with the Landau theory of ‘second order’ thermodynamic phase transitions.⁶

An example of such phenomena is the paramagnetic–ferromagnetic transition in a magnet close to its Curie point T_c . A_* then plays the role of

⁶An old but nice reference that exactly fits the present purpose is Section II of a review article by L.P. Kadanoff *et al.*, “Static phenomena near critical point: Theory and Experiment,” *Rev. Mod. Phys.* **39** (1967) 395–431. See also [Stanley (1988)].

the magnetization, the *order parameter* for that transition, and H is the magnetic field. Exponent $1/2$ in (4.13) and $1/3$ in (4.15) are the “classical” values of *critical exponents* β and $1/\delta$ linking the magnetization to the departure from T_c on the one hand, and the response to an applied field at $T = T_c$ on the other. Relation (4.14) defines a *susceptibility* that diverges as the inverse of the departure to criticality (critical exponent γ with classical value -1). Thermodynamic fluctuations slightly change the classical values that are easily derived from the Landau theory.

The notion of *universality* is central to the theory of so-called ‘critical phenomena’ associated to ‘macroscopic ordering’ measured by the order parameter. The values of the critical exponents involve only very general features of the system, especially the number of dimensions of physical space (usually 1, 2, or 3, for linear, planar, or bulk systems) and the symmetries of the order parameter. To stay with the magnetic example, the magnetization behaves as a vector with 1, 2, or 3 components, according to the existence of an easy direction (Ising model), an easy plane (XY model) or full isotropy (Heisenberg model), respectively.

The Landau theory can also deal with ‘first order’ transitions that are discontinuous, provided that an order parameter can be defined. For the liquid–gas transition, the order parameter is the density difference between the liquid and the gaseous phases.

The mathematical counterpart of Landau theory is Thom’s *catastrophe theory*, see e.g. [Poston and Stewart (1978)].

4.2.1.2 Emergence of periodicity

Increasing the complexity of the dynamics, we now consider the emergence of temporal oscillations, which requires a two-dimensional effective phase space, as already learned in Chapter 2. This phenomenon, called *Hopf bifurcation*, (or *Landau–Hopf*, *Hopf–Andronov*, *Poincaré–Andronov*) is best described through a complex representation of the relevant subspace where it develops. The generic model reads:

$$\dot{A} = sA - g|A|^2 A, \quad (4.16)$$

with $A \in \mathbb{C}$, $s = \sigma - i\omega$, and $g = g' + ig''$. Setting $A = \rho \exp(i\varphi)$, upon substitution and after simplification by $\exp(i\varphi)$ we get:

$$\dot{\rho} + i\rho\dot{\varphi} = (\sigma - i\omega)\rho - (g' + ig'')\rho^3$$

and, separating real and imaginary parts:

$$\dot{\rho} = \sigma\rho - g'\rho^3, \quad (4.17)$$

$$\dot{\varphi} = -\omega - g''\rho^2. \quad (4.18)$$

As already discussed, the coefficients in (4.16) are *a priori* functions of the control parameter r , but at the dominant order we can assume that ω and g are constant, and introduce the dependence on r only where it is indispensable, *i.e.* to control the growth rate. Since it must be negative below threshold (damping) and positive above (amplification), we can simply take $\sigma \propto r$.

The study of the problem for the modulus ρ is similar to that for the order parameter A in the previous section. Solving (4.17) for ρ at steady state (*i.e.* after elimination of the transient behavior), we get:

$$\rho = \rho_* = (\sigma/g')^{1/2} \quad (4.19)$$

which, once inserted in (4.18), yields:

$$\varphi(t) = -\omega_* t + \varphi_0 \quad \text{with} \quad \omega_* = \omega + g''r/g', \quad (4.20)$$

where φ_0 is a constant that depends on initial conditions. The so-obtained *limit cycle* is stable when the bifurcation is supercritical, which implies $g' > 0$, as illustrated in Figure 4.5. On the other hand, as understood from (4.20), coefficient g''/g' determines the change in angular frequency due to nonlinear couplings, *i.e.* the oscillation's nonlinear dispersion.

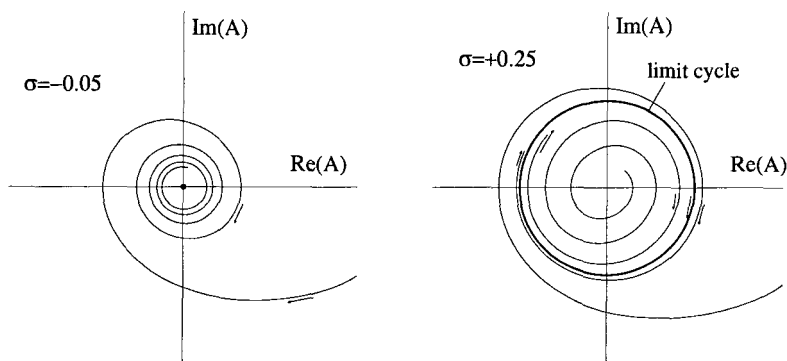


Fig. 4.5 Supercritical Hopf bifurcation (emergence of a stable limit cycle). The oscillations relax towards the origin below the threshold (left) and saturate at a finite amplitude above (right).

4.2.1.3 Dynamics in dimension two, general case

In fact one can show in full generality that the behavior of a system with a two-dimensional phase space which is isomorphic⁷ to \mathbb{R}^2 cannot have regimes that are more complicated than periodic according to the *Poincaré–Bendixson theorem*. A qualitative idea of the reason why complex behavior (chaos) is excluded for two-dimensional time-continuous systems stems from the observation that, at a regular point (*i.e.* $\mathcal{F}(\mathbf{X}) \neq 0$) the vector field defines only one tangent direction, so that two trajectories cannot cross at this point. In dimension 2, the consequence of this fact is particularly drastic: a trajectory is a line (dimension 1) that splits the space (dimension 2) in two disconnected parts. Once transported everywhere by the vector field, this topological constraint implies that trajectories corresponding to steady states can be either fixed points or closed curves, *i.e.* time-independent or time-periodic states. The rigorous mathematical proof of this result is not as easy as it seems; accessible references are [Hirsch and Smale (1974)] or [Lefschetz (1977)], for example. By contrast, many things become possible in dimensions strictly larger than two since trajectories have then enough room to wind in complicated ways without crossing by “escaping” in the supplementary dimensions.⁸

In what follows, we examine first the case of periodically forced two-dimensional systems, which are in fact three-dimensional systems with a particular structure. The stroboscopic analysis of trajectories (concretely illustrated in the numerical experiments of appendix B) is used to introduce discrete-time dynamical systems essential to the understanding of the subsequent transition steps toward chaos. Before doing this we examine first the respective roles of linear resonance and nonlinearity on the particularly simple case of the forced Duffing oscillator.

4.2.2 Quasi-periodicity and resonances

4.2.2.1 Forced systems

Up to now we have considered *autonomous systems* in which time t does not appear explicitly, so that the trajectory is independent of the instant chosen to specify the initial condition in phase space, which is no longer

⁷The surface of a torus is not isomorphic to \mathbb{R}^2 though tangent planes can be defined everywhere.

⁸The same will hold for two-dimensional manifolds with nontrivial topology such as the Möbius band, which cannot be applied on \mathbb{R}^2 without tear but can indeed be embedded in \mathbb{R}^3 , hence the third dimension.

the case of *forced systems* introduced on p. 27. It is easily seen that the effective dimension of a forced system formally written as:

$$\dot{\mathbf{X}} = \mathcal{F}(\mathbf{X}; t), \quad (4.21)$$

is increased by one with respect to the dimension of the corresponding unforced system. In order to specify a trajectory completely, we have indeed to choose not only the initial condition $\mathbf{X}^{(0)}$ but, since the system is no longer time-translationally invariant, to tell also the time $t^{(0)}$ at which we start the system. This very need for a supplementary initial condition already points to an increase of the effective dimension.

More formally, one can pass to an *extended phase space* in which the system is autonomous by introducing an auxiliary state variable U trivially governed by $\dot{U} \equiv 1$. Setting $\mathbf{Y} = \{\mathbf{X}, U\}$ we then obtain:

$$\dot{\mathbf{Y}} = \mathcal{G}(\mathbf{Y}) \quad \text{with} \quad \mathcal{G} = \{\mathcal{F}, 1\} \quad (4.22)$$

which is indeed autonomous. If the initial condition was $\mathbf{X} = \mathbf{X}^{(0)}$ at $t = t^{(0)}$ for (4.21), then for system (4.22), $U^{(0)} = t^{(0)}$ presents itself as the initial condition for U . The extended phase space is thus the product of the original phase space \mathbb{X} by \mathbb{R} which accounts for the time variable.

In practice, the most familiar case of non-autonomous system corresponds to *periodic forcing* with period T (angular frequency $\omega = 2\pi/T$), i.e. $\mathcal{F}(\mathbf{X}; t + T) = \mathcal{F}(\mathbf{X}; t)$. From a mechanical viewpoint, one can understand the supplementary variable U as characterizing the rotation of a wheel with a moment of inertia so large that its angular speed ω is independent of the state of the system to which it is coupled, acting on it like the connecting rod of a steam engine.

Stroboscopic analysis of the trajectories at the period of the forcing then comes to take pictures of the system at a series of times $t_k = kT$, $k \in \mathbb{N}$. Geometrically, this operation corresponds to a series of “sections” of the extended phase space (Figure 4.6, left). During the time interval between two sections, the trajectory can be computed with as much precision as desired by integration of (4.21).

Owing to the periodicity of the forcing, we can represent the full trajectory by registering the state of the system in its (reduced) phase space \mathbb{X} while keeping track of the instant it passes through this state using label k . In this perspective the full phase space of the system in restricted representation is the product of \mathbb{X} by the periodized interval $[0, T]$; the periodized interval $[0; 1]$ is usually called the one-dimensional sphere \mathbb{S}^1 , so that one

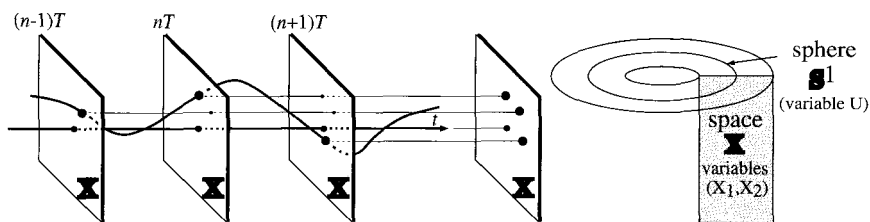


Fig. 4.6 Extended representation (left) and restricted representation (right) of the phase space of a periodically forced system. The stroboscopic analysis corresponds to a series of “sections” in the extended phase space, further identified modulo T in the restricted representation.

can denote it as $\mathbb{X} \oplus TS^1$ (Figure 4.6, right). The generalization of this operation to the case of autonomous dynamical systems (*Poincaré section*) is a particularly efficient tool for the understanding of the emergence of chaos.

4.2.2.2 Steady state of a periodically forced oscillator

Let us consider a Duffing oscillator with natural period $\omega_0 = 1$, damped but externally forced:

$$\ddot{X} + 2\eta\dot{X} + X + \varepsilon X^3 = f \cos(\omega t). \quad (4.23)$$

We consider here only the case of a saturating nonlinearity $\varepsilon \geq 0$ (see also Exercise 2.5.7).

• *Linear preliminary.* When $\varepsilon = 0$, after the damping of transients, the steady state response is obtained by inserting $X = A_f \cos(\omega t - \varphi)$ in (4.23), which yields:

$$[(1 - \omega^2) \cos(\omega t - \varphi) - 2\eta \sin(\omega t - \varphi)] A_f = f \cos(\omega t).$$

Expanding $\cos(\omega t - \varphi)$ and $\sin(\omega t - \varphi)$, by identification of terms in $\cos(\omega t)$ and $\sin(\omega t)$, we get:

$$\begin{aligned} [(1 - \omega^2) \cos \varphi + 2\eta \omega \sin \varphi] A_f &= f, \\ -2\eta \omega \cos \varphi + (1 - \omega^2) \sin \varphi &= 0. \end{aligned}$$

We derive immediately from the second equation that

$$\tan \varphi = \frac{2\eta\omega}{1 - \omega^2}, \quad (4.24)$$

and, upon elimination of $\cos \varphi$ and $\sin \varphi$

$$\left\{ (1 - \omega^2)^2 + 4\eta^2 \omega^2 \right\} A_f^2 = f^2, \quad (4.25)$$

which leads to

$$A_f = \frac{f}{\sqrt{(1 - \omega^2)^2 + 4\eta^2 \omega^2}}. \quad (4.26)$$

In Figure 4.7, this solution of the linear problem for $f = 1$, labelled $\varepsilon = 0$, is represented as a thick solid line for $\eta = 0.1$ and as a thin solid line in the limit $\eta = 0$.

• *Effect of the nonlinearity.* Let us assume that the forcing is sufficiently weak ($f \ll 1$) and that the response is not much distorted so that we can restrict ourselves to a first harmonic approximation, even close to the linear resonance. At steady state, we can still keep $X = A_f \cos(\omega t - \varphi)$ which, once inserted in (4.23), adds to the terms already obtained the quantity $\varepsilon A_f^3 \cos^3(\omega t - \varphi) = \varepsilon A_f^3 \left[\frac{3}{4} \cos(\omega t - \varphi) + \frac{1}{4} \cos(3(\omega t - \varphi)) \right]$. Only the first term of this sum is of interest to us now. Expanding it as before in $\cos(\omega t)$ and $\sin(\omega t)$, we immediately see that the solution can be obtained by replacing $(1 - \omega^2)$ by $[(1 - \omega^2) + \frac{3}{4} \varepsilon A_f^2]$ everywhere.

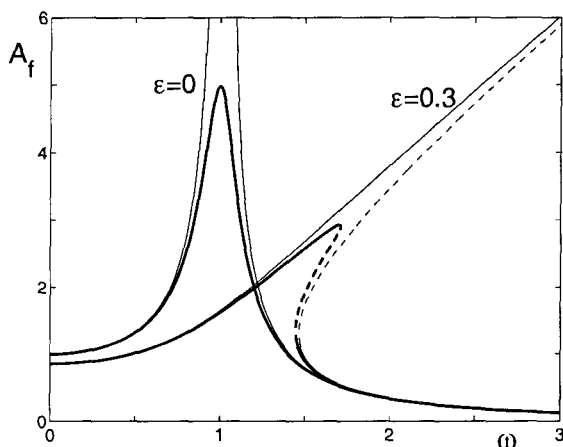


Fig. 4.7 Response A_f of the periodically forced Duffing oscillator upon sweeping the frequency around its resonance value. Thick and thin lines correspond to $\eta = 0.1$ and $\eta = 0$, respectively in the linear ($\varepsilon = 0$) and nonlinear ($\varepsilon = 0.3$) cases. Stable solutions are represented by solid lines and unstable ones by dashed lines.

Equation (4.25) now reads

$$\left\{ [(1 - \omega^2) + \frac{3}{4}\varepsilon A_f^2]^2 + 4\eta^2 \omega^2 \right\} A_f^2 = f^2. \quad (4.27)$$

This equation is cubic in A_f^2 and can thus generically have one or three solutions, by contrast with the linear case ($\varepsilon = 0$) for which the solution in A_f^2 is unique.

Expanding (4.27) and considering the sign of its coefficients, one can easily show that there is always at least one positive root in A_f^2 . In order to convince ourselves that it can also have other positive roots, we now examine the limiting case $\eta = 0$ which reads:

$$[(1 - \omega^2) + \frac{3}{4}\varepsilon A_f^2]^2 A_f^2 = f^2.$$

In the absence of forcing ($f = 0$), in addition to the trivial solution $A_f = 0$, this equation has the double root:

$$A_f^2 = A_0^2 = \frac{4}{3\varepsilon}(\omega^2 - 1), \quad (4.28)$$

which is acceptable as soon as $\omega \geq 1$ (for $\varepsilon > 0$, which we assume). This solution is perturbed by the introduction of a small forcing that suppresses the degeneracy. For ω sufficiently large, the pair of solutions that derives from it is given with a good approximation by

$$A_f^2 = A_0^2 \pm \tilde{A} \quad \text{with} \quad \tilde{A} = f[4(\omega^2 - 1)/3\varepsilon]^{-1/2},$$

where the correction \tilde{A} remains small when compared to A_0^2 , itself large in the considered limit $\omega \gg 1$. These two solution branches are traced for $f = 1$ and $\varepsilon = 0.3$ as thin lines in Figure 4.7. The solution for $f = 0$ derived from (4.28) is an arc of hyperbola (not drawn) that starts at $\omega = 1$ and serves as a common asymptote inbetween these two branches. The thick line corresponds to the solution of the equation (4.27) including the viscous friction term with $\eta = 0.1$. As usual, unstable solutions are indicated by dashes.

In applications, one can fix f and change ω , or the reverse. In both cases one observes that there exist ranges of parameters over which multiple solutions exist. Then there are three solutions, one can show by methods adapted from those developed in Chapter 2 that the solution with intermediate amplitude is unstable and thus cannot be observed. By sweeping the control parameter (angular frequency or amplitude of the forcing) one

may drive the system to perform hysteresis cycles during which the oscillator jumps from a large amplitude to a small one or the reverse. One can also notice that when the nonlinearity is saturating ($\varepsilon > 0$), the curves bend in the direction of high frequencies, which is easily understood from the relation between the amplitude and the angular frequency for the free oscillator, Equation (2.48) p. 52 (increased average amplitude implies increased effective stiffness and thus shortening of the period).

• *Secondary resonances.* The modification of the response curve in the neighborhood of the natural period of the oscillator, the so-called *primary* resonance is the most immediate effect of nonlinearity. The existence of *secondary* resonances at angular frequencies close to multiples or sub-multiples of this angular frequency is slightly less intuitive, though they still result from elementary trigonometric relations. The subharmonic resonance is most easily understood. As a matter of fact, if the forcing period $\omega = 1/3$ is apparently far from the resonance, the cubic nonlinearity induces some response at $\omega = 1$ since $\cos^3(t/3) = \frac{3}{4} \cos(t/3) + \frac{1}{4} \cos(t)$. In turn, this response can be seen as an external forcing of the fundamental mode, inducing its own resonant response. Considering a superposition $X = [A \cos(t + \psi) + A_f \cos(\omega t + \varphi)]$ and computing X^3 one finds terms in

$$\begin{aligned} &\cos^3(t + \psi), \quad \cos^2(t + \psi) \cos(\omega t + \varphi), \\ &\cos(t + \psi) \cos^2(\omega t + \varphi), \quad \cos^3(\omega t + \varphi), \end{aligned}$$

which generate terms with angular frequencies $\pm 1, \pm 3, \pm 2 \pm \omega, \pm 1 \pm 2\omega, \pm \omega$ et $\pm 3\omega$, where the \pm signs come from the fact that the resonance does not depend on the sign of the arguments of the sines and cosines. A resonance occurs every time a combined angular frequency is equal to the natural angular frequency (± 1).⁹ In addition to $\omega \approx 1$ corresponding to the primary resonance, this rule adds $\omega \approx 1/3$ ($3\omega = 1$), $\omega \approx 3$ ($2 - \omega = -1$), and of course $\omega \approx 0$. However the orders of magnitude of these different perturbations to the initial problem (the free, linear, frictionless oscillator) are different in each case, which imposes separate studies of lesser interest than that of the primary resonance.

• *Simple or complex response?* As in Chapter 2, if one wants to go beyond the first harmonic approximation, one has to develop rigorous perturbation approaches by multiple scale methods. In the present context this would however lead us too far with little compensation as far as the insight into

⁹Expanding the solution in terms of complex variables would lead to two conjugate resonance conditions, and at the end the same combinations, hence the ± 1 .

nonlinear phenomena is concerned. (Asymptotic approaches to nonlinear oscillations are examined in greater detail in [Nayfeh and Mook (1979)].)

In practice, the relative simplicity of the response of the Duffing oscillator with a saturating nonlinearity ($\varepsilon > 0$) submitted to a harmonic forcing stems from the fact that its phase space contains just one center at the origin and no unstable elements. This would no longer be the case if, instead of $\ddot{X} + X + X^3 = 0$, we had taken $\ddot{X} - X + X^3 = 0$. The study of its phase portrait similar to that in Exercises 2.5.6 and 2.5.8 shows that the center at the origin is replaced by a saddle and it is precisely the instability inherent in this type of fixed point which is at the origin of the chaotic behavior observed under external periodic forcing when the forcing increases beyond some threshold. More on this subject can be found in [Guckenheimer and Holmes (1983)], whereas the numerical study proposed in Appendix B, Section B.4.1, shows that the same result holds in the case of the periodically forced damped pendulum for the same reason: the presence of saddles in the phase portrait of the unperturbed system, Figure 2.9, p. 44).

Before entering the realm of chaos, let us consider the (still regular) case of self-sustained oscillations submitted to a periodic external forcing.

4.2.3 Quasi-periodicity and lockings

The phase portrait of the (unforced) van der Pol oscillator is less trivial than that of the standard damped Duffing oscillator since it displays an unstable focus at the origin and an attracting limit cycle surrounding it at some distance. We take it here in the form (2.60), p. 54 which, when externally forced, reads:

$$\ddot{X} - \varepsilon(1 - X^2)\dot{X} + X = f \cos(\omega t). \quad (4.29)$$

Its different regimes will systematically be studied by means of stroboscopic analysis at the forcing period $T = 2\pi/\omega$.

In the absence of forcing ($f = 0$), the temporal evolution of some observable $\mathcal{W}(\mathbf{X})$ function of the state $\mathbf{X} \equiv \{X, \dot{X}\}$ of the oscillator is a periodic function of time with period $T_0 = 2\pi/\omega_0$ ($\omega_0 \approx 1$ for $\varepsilon \ll 1$, see. §2.3.2.2, p. 52).

Assuming that the forcing is weak ($f \ll 1$) and that the imposed angular frequency is not commensurate with ω_0 , i.e. $\omega/\omega_0 = \alpha$ irrational, after transients have decayed we expect $\mathcal{W}(\mathbf{X}(t)) = G(\omega_0 t + \varphi, \omega t + \psi)$ with $G(u + 2\pi, v) \equiv G(u, v + 2\pi) \equiv G(u, v)$, i.e. two-periodic behavior.

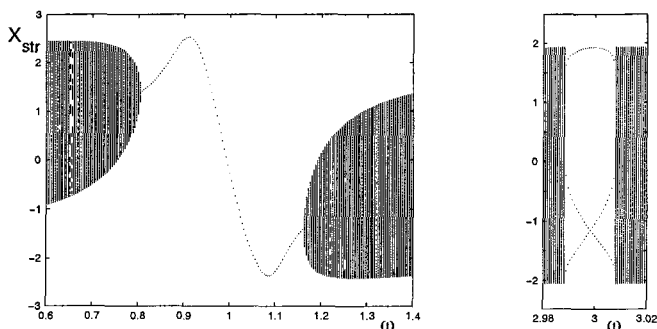


Fig. 4.8 Bifurcation diagram of the forced van der Pol oscillator. Left: $\omega \approx 1$, $\varepsilon = 0.1$, and $f = 0.5$. Right: $\omega \approx 3$, $\varepsilon = 0.1$, and a larger forcing, $f = 1.0$, to make its effects more visible. Notice also the expanded scale for ω .

By contrast, when ω and ω_0 are commensurate, *i.e.* $\omega/\omega_0 = \alpha \in \mathbb{Q}$, $\alpha = p/q$, integers p and q being relative primes, $\mathcal{W}(\mathbf{X})$ is a periodic function of time with period equal to the smallest common multiple of T and T_0 , $\tilde{T} = pT = qT_0$.

- *Frequency locking.* When the intensity of the forcing increases, the oscillator can “feel better” if it leaves its own frequency and adopts that of the forcing. It is the *locking* phenomenon: over a full range of values of ω , around a condition such that $qT_0 = pT$, the oscillator adjusts its motion so that its effective period \tilde{T}_0 , *a priori* function of f and $\omega = 2\pi/T$, still fulfills the resonance condition, $q\tilde{T}_0 = \tilde{T} = pT$ so that the period of the forced system remains \tilde{T} .

Figure 4.8 displays the set of stroboscopic recordings X_{str} as a function of the forcing frequency ω (bifurcation diagram) in a given numerical simulation of (4.29), thus illustrating this spectacular persistence phenomenon of *locking windows* for $\omega \approx 1$ with $\varepsilon = 0.1$ and $f = 0.5$ (left), and for $\omega \approx 3$ with $\varepsilon = 0.1$ and $f = 1.0$ (right).

Let us consider first the window at $\omega \approx 1$. When the locking takes place, the system is periodic with period T so that, when stroboscopically sampled at period T , it takes one and a single value $X_{\text{str}}(\omega)$. On the contrary, as soon as ω gets out of the window, though the oscillator is still sensitive to the forcing, it recovers its independence and the signal becomes two-periodic. The stroboscopic analysis then produces a picture such as that for $\omega = 0.75$ in Figure 4.9 (left): the state of the oscillator (X and \dot{X}) is registered at increasing multiples of the forcing period, $t_k = kT$,

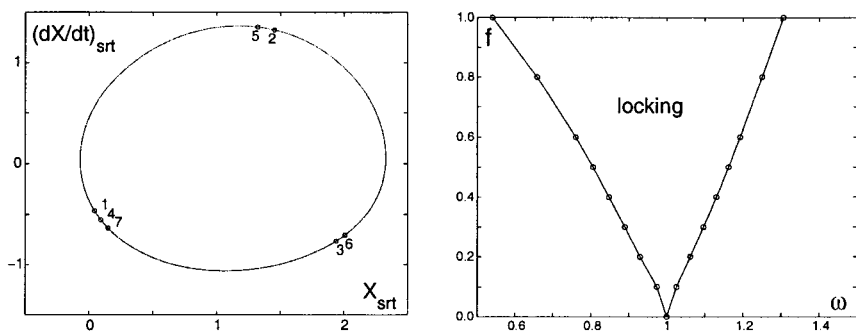


Fig. 4.9 Left: Stroboscopic analysis of a trajectory of the forced van der Pol oscillator for $\omega = 0.75$ and $f = 0.5$ (two-periodic unlocked regime). Right: Main resonance tongue $\omega \approx 1$: region of the (ω, f) parameter plane where locking is observed.

and it can be observed that the corresponding points arrange themselves along a closed curve that is continuously covered. Considering successive points shows that they jump from one position to the next with a slight shift, which explains the continuous coverage due to incommensurability of the two periods (while only a finite set of points would be reached in case of locking). The projection of this curve on the X axis produces the full vertical segments shown at values of ω corresponding to unlocked behavior on the bifurcation diagram of Figure 4.8. Notice that with $\omega = 0.75$ one has $4T_0 \simeq 3T$, i.e. close return every three samplings, which explains the proximity of points labelled 1, 4, and 7, etc.

The case of the window at $\omega \approx 3$ (Fig. 4.8, right) is analogous but, inside, we now have three values of X_{srt} for each ω . This is easily understood from the fact that the trajectory is sampled at period T which is about $1/3$ of the natural period of the oscillator, so that it is regularly sampled three times during one of its own turns. In the locked regime, it returns exactly at the same places (modulo 3) whereas outside the window, in the unlocked regime, return points shift slightly from one sampling to the next, which again gives continuous segments on the bifurcation diagram. Notice that, in spite of a much stronger forcing, the window is extremely narrow.

- *Emergence of complex behavior.* The variation of the range in ω where the van der Pol oscillator is locked to the forcing, the so-called *resonance tongue*, is displayed in Figure 4.9 (right) as a function of the intensity f of the forcing (on the vertical axis). For this resonance, it widens linearly with f at least as long as it is sufficiently weak. Higher order resonances

are narrower and widen more slowly. Frequency locking is a profoundly original manifestation of nonlinear effects. In the case of the van der Pol oscillator in a quasi-harmonic regime ($\varepsilon = 0.1$) it seems that one cannot observe phenomena more complicated than a decay of two-periodic behavior into simply periodic behavior, as long as one stays with reasonable values of the parameters. Things are different when the oscillator is more anharmonic (e.g. $\varepsilon = 1.0$). A wide variety of behaviors can be observed, with whole ranges of angular frequency where the response to forcing is chaotic, especially when the periodic driving is slow.

- *Mutual locking.* Up to now we have considered forcing in a strict sense, that is to say without feedback of the forced oscillator on the driving system. Besides, it is the presence of this immutable clock that makes the stroboscopic analysis easy to perform. Relaxing this condition, we can consider a system composed of two weakly coupled oscillators. Transposing the observations above, we may expect mutual locking in the neighborhood of resonance conditions fulfilled by the angular frequencies of these oscillators, for example Huygens' twin pendulum clocks.¹⁰ A system of two coupled oscillators is, as a whole, a four-dimensional system, each subsystem being two-dimensional. We are thus lead back to the case of autonomous systems in a dimension greater than two, to which we devote the end of this section.

4.2.3.1 Stability of a limit cycle: general case

To reach a higher complexity level, we must study the stability of self-sustained oscillations corresponding to limit cycles in phase space. This study must be performed not only on the surface containing the cycle, locally represented by the complex plane ($A \in \mathbb{C}$), which allows only perturbations in the radial direction, see Eq. (4.17), but in the full space in which the cycle is embedded, which permits "escape" in the supplementary dimensions. At this stage, it is useful to recall that we have arrived to an effective two-dimensional dynamics by adiabatic elimination of all stable modes, leaving us with a single relevant pair of center modes. Upon increasing the stress applied to the system, we have to consider the possibility that among stable modes, some become "dangerous." Mathematically speaking, the situation is more complex than before when we had to deal with a fixed point, since now we have to perturb a well established periodic dynamics.

¹⁰See the article by J. Whitfield, "Synchronized swinging," *Nature Science Update*, <http://www.nature.com/nsu/020218/020218-16.html>

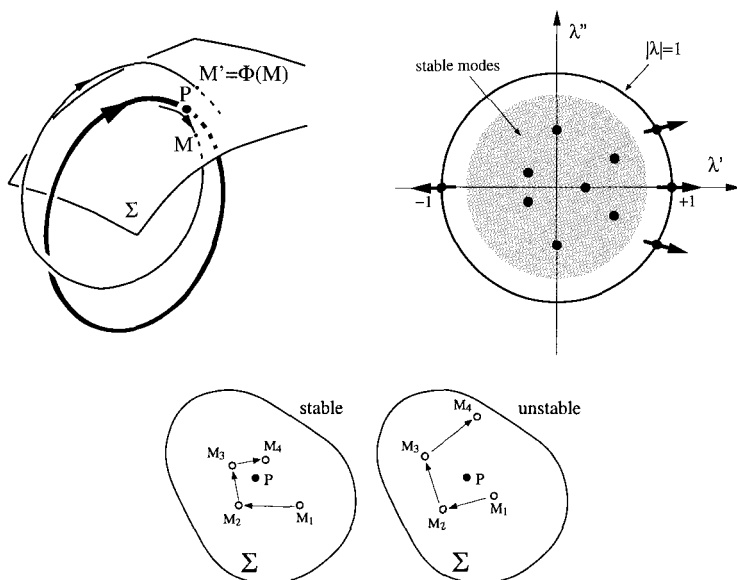


Fig. 4.10 Stability of a limit cycle from a geometrical viewpoint. Top-left: Poincaré section and first return (Poincaré) map $\Phi(M)$. Top-right: Spectrum of the linearized map Λ . Bottom: Stability/instability of the fixed point of the map.

Let us keep the geometrical approach sketched in Figure 4.6 illustrating the case of a periodic forcing, but now consider the intersections of the trajectories in a d -dimensional phase space with a $(d-1)$ -dimensional surface Σ , called the *Poincaré surface of section*, see Figure 4.10 (top-left). The oscillation that has settled can be viewed as a forcing for all other perturbations, and in the vicinity of the cycle, the phase space has indeed this product structure of the sphere S^1 times a relevant space in which “transverse” perturbations live, as extrapolated from Fig. 4.6 (right). A correspondence between successive intersections of trajectories with Σ is thus established in the form of a map of Σ onto itself $M' = \Phi(M)$, called the *first return map* or the *Poincaré map*. This transition from a continuous-time dynamics to a discrete-time one, from a d -dimensional differential system to a $(d-1)$ -dimensional map, is therefore basically similar to the stroboscopic analysis used for periodically forced systems. The difference just comes from the fact that the time interval between two sections is no longer the external forcing period but varies slightly with the position in the neighborhood of the cycle and tends to the period of the cycle as it is approached. Saying

this simply assumes that the differential dynamical system is smooth, so that the properties of the trajectories vary continuously, and that the surface of section is transverse (*i.e.* not tangent) to the cycle, so that the trajectories are correctly sampled.

Obviously, the cycle is associated with a fixed point \mathbf{P} of the map Φ (*i.e.* $\mathbf{P} = \Phi(\mathbf{P})$) and will be stable if \mathbf{P} is stable for Φ . In the neighborhood of \mathbf{P} , the map Φ can be linearized into an operator represented by a square $(d-1) \times (d-1)$ matrix Λ , and the stability properties of the cycle can be derived from its spectrum, as illustrated in Figure 4.10 (top-right).

In full generality, one expects non-degenerate complex eigenvalues and corresponding two-dimensional invariant subspaces that are easier to parameterize using complex variables. In such a subspace, the linearized dynamics then reads:

$$Z_{k+1} = \lambda Z_k, \quad (4.30)$$

$Z \in \mathbb{C}$ measuring the departure from the fixed point in the eigenspace of eigenvalue λ .

According to the definition, we have stability when the successive iterates of some initial condition $Z^{(0)}$ approach the origin as k increases and instability when they get away, Figure 4.10 (bottom). A given complex eigenmode is thus stable when $|\lambda| < 1$, marginal when $|\lambda| = 1$, and unstable when $|\lambda| > 1$. Writing λ as

$$\lambda = \rho \exp(2\pi i \alpha),$$

leads to a clear separation of the modulus ρ from the phase $\pm 2\pi\alpha$ of the eigenvalues.

The quantity α specifies the angular frequency of the mode that makes the cycle possibly unstable: $\alpha = \omega/\omega_0$. This can be irrational or rational like in the case of periodic forcing. Cases when $\lambda \in \mathbb{R}$ are special. Equation (4.30) then turns into a real iteration:

$$X_{k+1} = \lambda X_k, \quad (4.31)$$

and we must distinguish the dynamics corresponding to $\lambda > 0$ (*i.e.* $\alpha = 0$) for which iterates tend to or depart from the origin in a monotonic fashion from that observed when $\lambda < 0$ (*i.e.* $\alpha = 1/2$) for which they evolve by jumping alternatively from one side to the other.

Eigenvalue λ can be complex or not, but the corresponding stability condition remains $|\lambda| < 1$ and a bifurcation takes place when at least one

(pair of) eigenvalue(s) leaves the interior of the unit disc as the control parameters are varied. Different possibilities are indicated by arrows in Figure 4.10 (top-right).

Though the main purpose of the course is not a mathematical study of the different scenarios of transition to chaos in the perspective opened by Ruelle and Takens (see Figure 3.5, p. 93), let us mention that one can account for the simplest cases by completing (4.30) or (4.31) with appropriate terms. In the original Ruelle–Takens scenario, the destabilization of the limit cycle still leads to a regular but two-periodic regime ($\lambda \in \mathbb{C}$). The iteration that accounts for it reads

$$Z_{k+1} = \lambda Z_k - \gamma |Z_k|^2 Z_k, \quad \gamma = \gamma' + i\gamma'' . \quad (4.32)$$

After the damping of transients, it yields iterates evolving around a circle with radius $\sqrt{\rho - 1}$, where $\rho = |\lambda|$, Fig. 4.11 (top). Trajectories in phase space wound on an invariant *limit torus* which is the Cartesian product of two circles, one corresponding to the unstable limit cycle (longitude) and

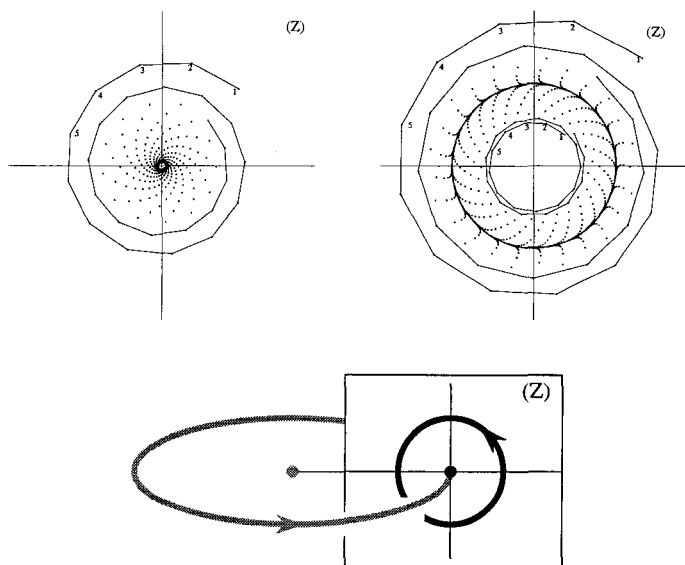


Fig. 4.11 Hopf bifurcation for a map (also called Neimark–Sacker bifurcation). Top: Iteration (4.32) for $|\lambda| < 1$ (left) and $|\lambda| > 1$ (right). Bottom: Perspective sketch of the skeleton of the *torus* over which the two-periodic dynamics develops asymptotically in time beyond bifurcation.

one for the new mode (meridian section), Fig. 4.11 (bottom), correspond to this description on the Poincaré surface.

The picture obtained in this case is very similar to that for the forced van der Pol oscillator. The difference is just that the two angular frequencies in the system now have intrinsic origin, the first one, which plays the role of the forcing, is that of the original cycle and the second one is that of its most dangerous instability mode. They can easily be identified on the records of physical observables, *e.g.* the two-periodic regime observed in convection and illustrated in Figure 3.8. As before, two-periodicity is observed only in the absence of resonant interaction between the two angular frequencies, that is to say as long as the ratio α remains irrational. Nonlinear couplings are therefore expected to be responsible for lockings when α approaches a rational value p/q as the control parameters are varied, lockings all the more visible when the denominator q is a small integer.

Two-periodic states, and *a fortiori* locked one-periodic states, are regular asymptotic regimes. In order to observe a chaotic behavior, it seems natural to think of an effective dimension still increased by one. This was precisely the context of the Ruelle and Takens approach, introducing *strange attractors* with properties accounting for irregularity in spite of determinism. More precisely, these authors showed (Note 8, p. 92) that when the system is smooth (C^∞), chaos is generic after supplementary bifurcations introducing two new angular frequencies in the system. The analyticity condition was later made milder (*i.e.* C^2 instead of C^∞) with chaos possibly occurring in three-frequency quasi-periodic systems.¹¹ However, concrete scenarios from two-periodic regimes to chaos generally rely on different explanatory models which would lead us on mathematical grounds too far away from our main purpose. On the other hand, it is more interesting to spend some time to consider resonant cases.

When $\alpha = p/q$ the two periods are resonant. Little is changed if q is large, *i.e.* $q \geq 5$. The resonance is *weak*) and the system behaves roughly as in the non-resonant case: typically, the dynamics still takes place on the torus that has emerged from the bifurcation. Genuinely two-periodic unlocked regimes alternate with locked regimes inside narrow tongues as the control parameters are varied. In a quasi-periodic state the trajectory winds on the torus without closing (the torus is densely covered with it), whereas in case of locking the trajectory is a closed cycle wound on the torus, making p turns along the meridian and q turns in the longitudinal

¹¹S. Newhouse, D. Ruelle, and F. Takens, "Occurrence of strange axiom A attractors near quasi-periodic flows on T^m , $m \leq 3$," Commun. Math. Phys **64** (1978) 35.

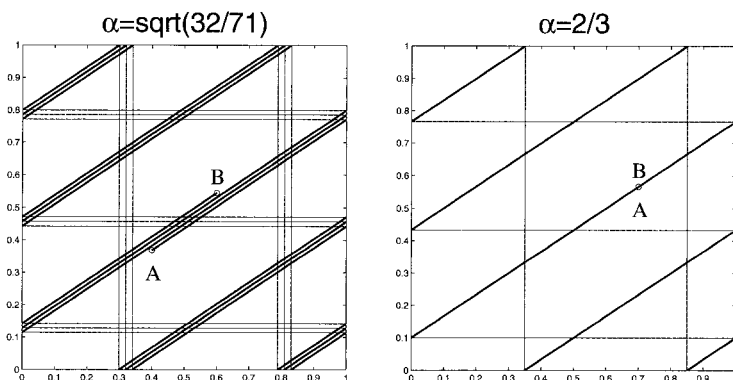


Fig. 4.12 Trajectories on the torus are represented by their phases: Longitude $\theta = \omega_0 t + \theta^{(0)}$ (horizontal axis) and meridian coordinate $\varphi = \omega t + \varphi^{(0)}$ (vertical axis) defined modulo 2π . Up to a factor 2π , the torus is isomorphic to the square $\theta \in [0; 1]$, $\varphi \in [0; 1]$ with opposite sides identified. Left: For a two-periodic state, $\alpha \notin \mathbb{Q}$, the whole (θ, φ) square is covered by any given trajectory as $t \rightarrow \infty$, here $\alpha = (32/71)^{1/2} = 0.671345 \dots$. Right: When $\alpha = p/q$, the same state is reached after a time $qT_0 = pT$, here $\alpha = 2/3 = 0.666666 \dots$ (Notice that $\alpha = 2/3$ is in principle a case of strong resonance; this value has been chosen here only because the figure is easy to read.)

direction (Fig. 4.12). Chaos may enter after a new instability mode sets in.

By contrast, when $q \leq 4$ the resonance is *strong* and has marked effects, destroying the torus over which the motion takes place. Most extreme cases correspond to $q = 2$ and $q = 1$ that bring back the map from a complex iteration (4.30) to a real iteration (4.31) since for $p/q = 1/2$ one has $\lambda = \exp(i\pi) = -1$ and for $p/q = 1/1$, $\lambda = \exp(2i\pi) = 1$. Each of these two cases govern a specific scenario.

- The *subharmonic cascade* observed in convection (Fig. 3.7) corresponds to the strong resonance $\alpha = 1/2$, whose normal form reads:

$$X_{k+1} = f_r(X_k) = -(1+r)X_k - X_k^3. \quad (4.33)$$

The corresponding scenario is illustrated here using the so-called *logistic map*¹²

$$X_{k+1} = 4rX_k(1 - X_k), \quad (4.34)$$

with $0 \leq r \leq 1$. The full bifurcation diagram in Figure 4.13 displays how the attractor (values of X reached as the iteration proceeds, after elimination

¹²For an introduction, see R.M. May, "Simple Mathematical models with very complicated dynamics," *Nature* **261** (1976) 459–467.

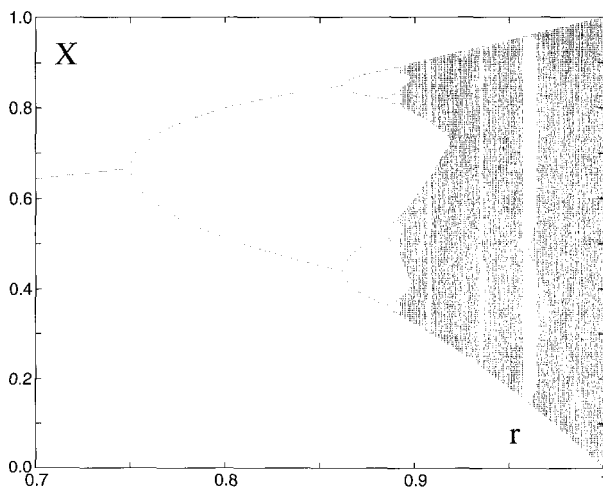


Fig. 4.13 Subharmonic cascade for (4.34).

of transients) changes as the control parameter r is varied.

For $r < 3/4$, a single point is obtained, corresponding to a periodic trajectory with period one (period T_0 if one considers the underlying limit cycle). At $r = r_1 = 3/4$ a first period-doubling takes place: a period-two regime sets in with two values X_1 et X_2 alternatively visited as the system evolves. (Working out the nonlinear variable change that turns (4.34) into the normal form (4.33) close to the bifurcation point is an interesting exercise.)

At $r = r_2 = 0.86237 \dots$, this period-two attractor is destabilized against a period-four regime, *etc.*, as observed in convection experiments (Fig. 3.7, p. 95). The bifurcation cascade ends up at $r = r_\infty = 0.89248 \dots$, where the system becomes periodic with infinite period in the form 2^{2^n} , $n \rightarrow \infty$. At this value, the so-called *margin of chaos*, the system is in fact aperiodic since it never returns exactly in the same state.

Beyond r_∞ , continuous vertical segments, in fact densely covered with points, are observed on the bifurcation diagram for each value of r . They are the trace of chaotic attractors for which infinite sets of unequally distributed points are visited all along a trajectory.

In fact, the situation is also very complicated in the parameter space since the return to periodic attractors is clearly visible in some parameter windows, the corresponding periodic states themselves decaying to chaos

through subharmonic cascades. Programming (4.34) or its variant (4.69), p. 175, is so easy that one should not miss exploring their bifurcation diagram numerically by oneself.

- *Intermittency* (type I, that featured in Figure 3.9, because several other types exist) takes place at a 1/1-resonance generically accounted for by the map:

$$X_{k+1} = r + X_k + X_k^2. \quad (4.35)$$

Before the transition, as long as $r < 0$, it has two fixed points solutions of:

$$X_{\pm} = r + X_{\pm} + X_{\pm}^2 \Rightarrow X_{\pm} = \pm\sqrt{-r}.$$

All trajectories starting with $X < X_{(+)}$ (and small enough) converge towards the fixed point at $X_{(-)}$. Other trajectories leave this limited region of phase space, Figure 4.14. Beyond the transition, for $r > 0$, the fixed points have disappeared but the local structure of phase space keeps a track of their presence as “ghosts”: iterates go through the kind of tunnel opened between the graph of the map and the line $X_{k+1} = X_k$. They move very slowly since $X_{k+1} = X_k$ plus some tiny correction, approach the origin and then go away.

Now the *global* structure of phase space may provide the opportunity for trajectories visiting remote regions of phase space to come in the neigh-

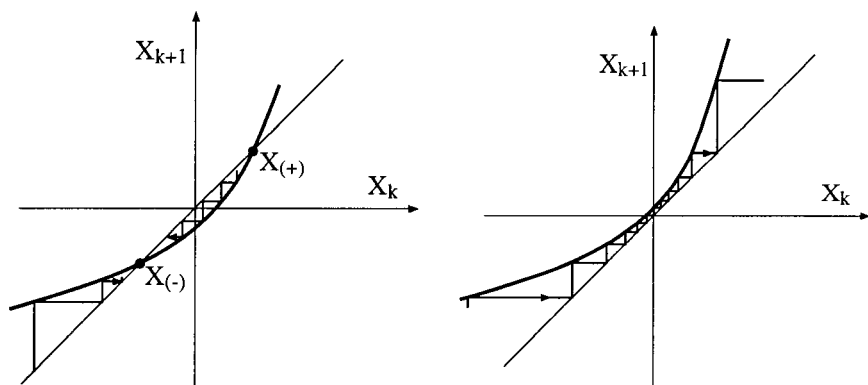


Fig. 4.14 Type-I intermittency according to (4.35). Left: $r < 0$, two fixed points, $X_{(-)}$ stable, $X_{(+)}$ stable. Right: $r > 0$, no fixed points but a narrow tunnel between the graph of the map and the line $X_{n+1} = X_n$.

borhood of the origin. When this is the case, for $r < 0$ the system coming close to the stable fixed point eventually converge to it. By contrast for $r > 0$ fixed points no longer exist, iterates sent in the vicinity of the origin, travel slowly through the tunnel, then get away and come back later, hence the intermittent behavior observed in Figure 3.9, p. 97.

Laminar intermissions are uncorrelated and their durations are unpredictable. This is due to the more or less uncontrolled evolution far from the previously existing limit cycle which generates randomness in the re-injection process.

While interpreting the experiments, one must remember that the map describes what happens after an appropriate section of the dynamics has been performed. At the bifurcation, twin limit cycles, one stable and the other unstable, collide and disappear. Laminar intermissions are made of slowly evolving regular periodic oscillations corresponding to the “ghost” limit cycles. They are interrupted by chaotic bursts during which the system explores remote regions in phase space, until it is sent back in the laminar region, ready for a new intermission.

4.3 Characterization of Chaotic Regimes

As conceived by Ruelle, *chaos* is a dynamical regime characterized by a specific *sensitivity* of trajectories to *initial conditions* and small perturbations. In phase space, it is accounted for by *strange attractors* that are robust attracting limit sets on which small departures between two trajectories are indefinitely amplified (the general meaning of instability) as a result of a stretching-and-folding process analogous to the making of Danish pastry (baker map, see later Figure 4.17).

The main interest of these concepts is to reconcile *determinism* and *stochasticity* in dissipative dynamical systems, which was initially supposed to further shed some light on the problem of the “nature of turbulence” as discussed in Chapter 3, §3.2.2.3, p. 92.

In this section we thus focus on a quantitative estimate of the two main facets of chaotic dynamics: the “longitudinal” instability measured by *Lyapunov exponents* and the *fractal dimensions* characterizing the “transverse” foliated structure.

4.3.1 Instability of trajectories and Lyapunov exponents

The instability of trajectories on a strange attractor is illustrated here by means of an everywhere expanding iteration called the *dyadic map* (Fig. 4.15, top-left). It reads:

$$X_{k+1} = 2X_k \pmod{1}. \quad (4.36)$$

It is convenient to visualize the trajectory $\{X_k, k = 0, 1, \dots\}$ as a walk in the complex plane $Z_{k+1} = Z_k + \exp(2\pi i X_k)$. (Z has no dynamical significance here by contrast to X which is governed by the map.) This simple

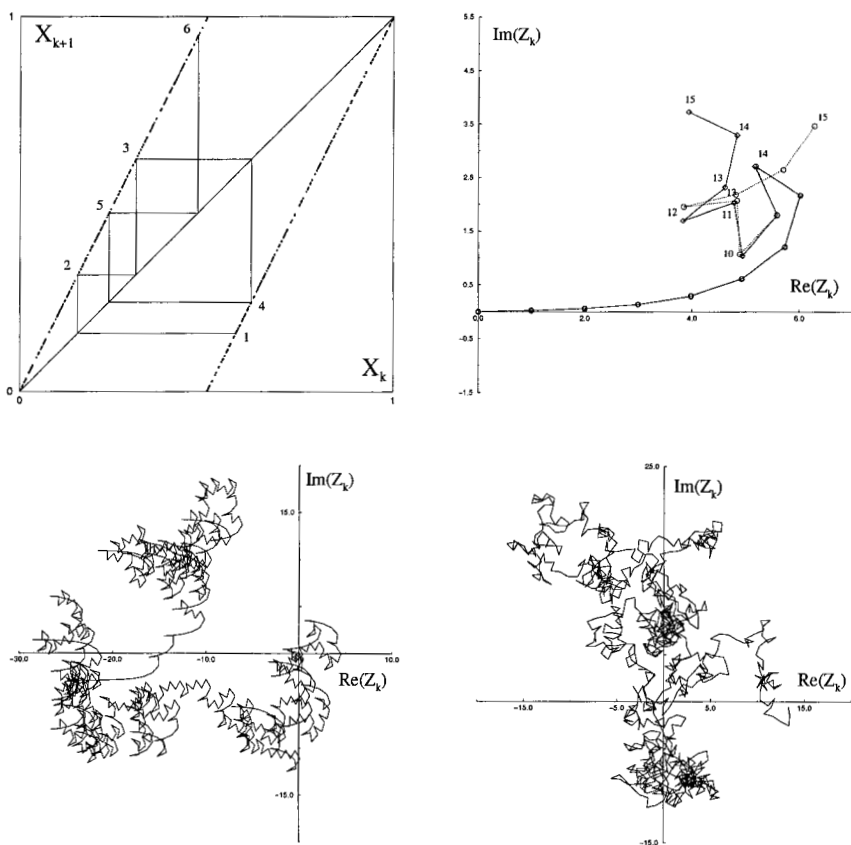


Fig. 4.15 Interpretation of chaos. Top left: Dyadic map. Top right: Divergence of neighboring trajectories. Bottom left: Dyadic walk. Bottom right: Random walk.

representation helps us to clearly illustrate the divergence of trajectories starting at neighboring points (Fig. 4.15, top-right) and the long-term evolution (Fig. 4.15, bottom-left) that leads one to think of the random walk that would be obtained by drawing the successive X_k uniformly at random over the unit interval (Fig. 4.15, bottom-right).

The divergence rate of trajectories is a good measure of chaotic behavior. Let us show how the analysis proceeds in a simple example and consider a map f of a single real variable X :

$$X_{k+1} = f(X_k),$$

more general than (4.36). To begin with, a given trajectory $\{X_k; k = 0, 1, 2, \dots\}$ starting at $X_0 = X^{(0)}$ is taken as a reference and we consider a neighboring trajectory $\{\tilde{X}_k; k = 0, 1, 2, \dots\}$ starting at $\tilde{X}_0 = X^{(0)} + \delta X_0$. Denoting $f' = df/dX$ we have:

$$\begin{aligned}\tilde{X}_1 &= X_1 + \delta X_1 = f(X_0 + \delta X_0) = f(X_0) + f'(X_0) \delta X_0 \\ \Rightarrow \quad \delta X_1 &= f'(X_0) \delta X_0\end{aligned}$$

and using the chain rule:

$$\delta X_k = \left(\prod_{m=0}^{k-1} f'(X_m) \right) \delta X_0.$$

Assuming a geometrical growth/decay as $|\delta X_k| \sim \gamma^k |\delta X_0| \equiv \exp(k\lambda) |\delta X_0|$, which defines both γ and $\lambda = \ln \gamma$, we get:

$$\gamma = \left(\left| \frac{\delta X_k}{\delta X_0} \right| \right)^{1/k} = \left(\prod_{m=0}^{k-1} |f'(X_m)| \right)^{1/k}.$$

At this stage, γ still depends on k . To get rid of this dependence we take the limit $k \rightarrow \infty$ which leads to the definition of the *Lyapunov exponent*:

$$\lambda = \ln(\gamma) = \lim_{k \rightarrow \infty} \frac{1}{k} \sum_{m=0}^{k-1} \ln(|f'(X_m)|). \quad (4.37)$$

In other words, the Lyapunov exponent is thus the time average of the local divergence rate $\ln(|f'|)$, *i.e.* a measure of long term *unpredictability*. Trajectories diverge in the mean when $\lambda > 0$, which can be taken as the definition of a chaotic dynamics. For the dyadic map (4.36), one gets $\lambda = \ln 2 > 0$.

The extension to maps with several variables leads to the definition of the *Lyapunov spectrum*, which rests on the analysis of the asymptotic behavior of the product of Jacobian matrices obtained from the chain rule. This generalizes the eigenspectrum of the stability matrix at a fixed point to the case of arbitrary trajectories. Technically, the matter is difficult but, in the limited context of this course, it is sufficient to know that this can be done and that, by successive generalizations, one can determine Lyapunov spectra for differential systems (from time- τ maps, see p. 28) and for continuous media governed by partial differential equations (after spectral approximation or discretization leading to finite-order ordinary differential systems, see Appendix B).

The Lyapunov spectrum can be ordered by decreasing values of the individual exponents. The system is then declared to be chaotic when the largest exponent is positive. The empirical determination of Lyapunov exponents from time records will be examined later, p. 165.

Let us stress the fact that the whole approach in terms of dynamical systems is a progressive extension of linear instability concepts from time-independent regimes (fixed points of continuous-time systems) to periodic regimes (limit cycles then seen as fixed points of discrete-time systems) and finally to irregular aperiodic regimes.

4.3.2 Fractal aspects

Up to now we have been interested in expansion properties “along” the attractor. However the systems of interest are supposed to be dissipative, which implies overall contraction of volumes in phase space. As we have seen, chaotic behavior is marked by instability, which means expansion in some directions. This expansion has to be more than compensated for by stronger contraction in other directions. Some folding must then take place in order to maintain trajectories in a bounded region of the phase space, as sketched in Figure 4.16. (The case of regular regimes would be much less anisotropic with, at most, neutral directions on average.)

What happens in the “transverse directions” can be concretely illustrated using a celebrated simple two-dimensional map called the *baker map* (Fig. 4.17, top-left). This map of the unit square $[0, 1] \times [0, 1]$ expands it onto itself by a factor $\kappa = 2$ in the direction of the first coordinate and by a factor $\kappa' = \alpha/\kappa$ in the other direction ($\kappa' < 1 \Rightarrow$ contraction).

When $\alpha = 1$, that is $\kappa' = 1/2$, the baker’s map is conservative (areas are preserved). In order to obtain a dissipative system, contraction must

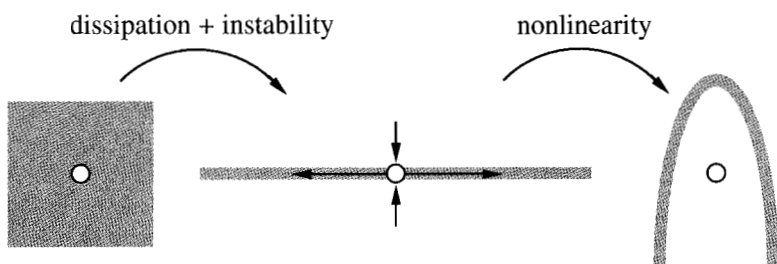


Fig. 4.16 Expansion in unstable direction, contraction due to dissipation, folding by nonlinearities, all in combination, produce *horseshoes* typical of chaotic attractors.

be larger than expansion, *i.e.* $\alpha < 1$, so that $\kappa\kappa' = \alpha < 1$. The strange attractor obtained in that case displays a characteristic *fractal* transverse structure (Fig. 4.17, top-right). This fractal structure is a triadic *Cantor set* classically obtained by removing the middle third of a segment and repeating indefinitely the operation on the two segments left apart in that operation as shown in Figure 4.17 (bottom), yielding a self-similar set that is invariant upon magnification by a factor of three.

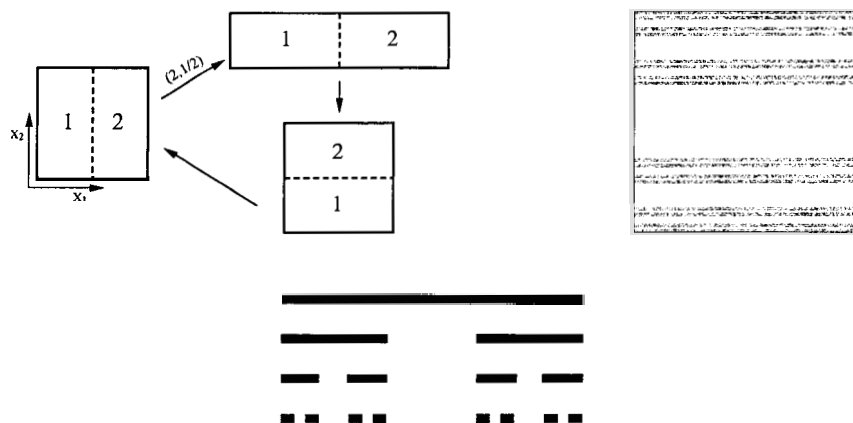


Fig. 4.17 Top-left: Conservative *baker map* (1st step: expand along X_1 ($\kappa = 2$) and contract along X_2 ($\kappa' = 1/2$); 2nd step: cut right half of rectangle and place it back in square). Top-right: Strange attractor for the dissipative map with $\kappa' = 1/3$ (expansion rate $\kappa\kappa' = 2/3 < 1$). Bottom: Few steps of the construction rule of the triadic Cantor set, to be read from right to left. (Notice that, to build the dissipative baker attractor, we used a map that translates part (2) above part (1) and puts it upside down so that the fractal structure follows from the conventional Cantor middle-third rule.)

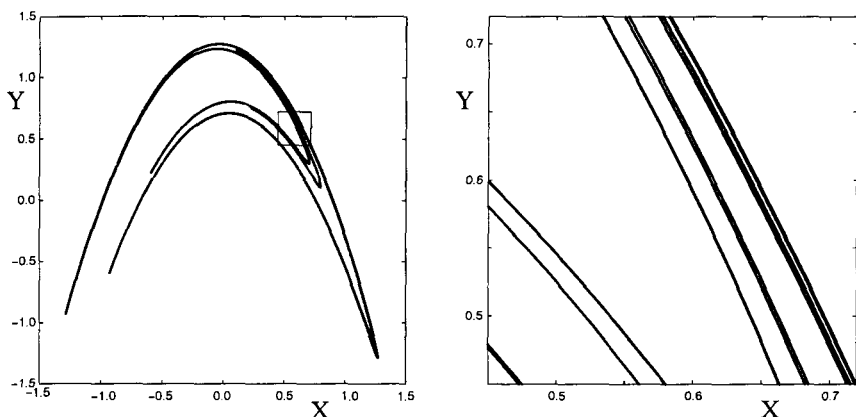


Fig. 4.18 Hénon attractor obtained by iterating map (4.38, 4.39) for $a = 1.4$ and $b = 0.3$ from some initial condition after elimination of the transient. Left: The full attractor. Right: Zoom on the boxed region.

In practice, nonlinearities usually fold the trajectories as seen with the Hénon map:¹³

$$X_{k+1} = 1 - aX_k^2 + bY_k, \quad (4.38)$$

$$Y_{k+1} = X_k. \quad (4.39)$$

The attractor corresponding to $a = 1.4$ and $b = 0.3$ is presented in Figure 4.18. The folding originates from the nonlinearity in (4.38), which is of “logistic” type (see Exercise 4.6.9). Coefficient b in (4.39) guarantees the dissipative character of the map provided that $|b| < 1$, as shown by performing Exercise 2.5.1 with this map. The fractal character of the attractor is particularly obvious from the magnification of the boxed region displayed in the right part of the figure.

The *fractal dimension* gives a good idea of the way the attractor occupies the phase space. In a d -dimensional space, it is obtained by covering the considered set, here the attractor, by elementary volume elements of size ε^d , next counting the number $\mathcal{N}(\varepsilon)$ of such elements necessary to cover it, and finally study how that number grows as the linear size ε of the volume elements tends to zero. The fractal dimension d_f is thus defined through

¹³M. Hénon, “A two-dimensional mapping with a strange attractor,” Commun. math. Phys. **50** (1976) 69.

the formula:

$$d_f = \lim_{\varepsilon \rightarrow 0} \frac{\log(\mathcal{N}(\varepsilon))}{\log(1/\varepsilon)}. \quad (4.40)$$

For an ordinary, connected, continuous set, this definition yields the usual *topological dimension* (0 for a point, 1 for a line, 2 for an ordinary surface, *etc.*). Let us see how it works for an indefinitely fragmented object like the triadic Cantor set by considering it at step k of the construction process. It can be covered by segments of length $\varepsilon = 1/3^k$, and 2^k such segments are needed at that step, hence:

$$d_f(k) = \frac{\log(2^k)}{\log(1/(1/3)^k)} = \frac{\log(2)}{\log(3)} \approx 0.63092975,$$

somewhere between the dimension of a countable set of isolated points (0) and that of a continuous segment (1).

Here the evaluation does not depend on k because the set is strictly self-similar but more generally the limit $\varepsilon \rightarrow 0$ must really be taken. The computation of the fractal dimensions of other classical self-similar sets from a direct application of (4.40) is the subject of exercise 4.6.12.

Turning to the dissipative baker map, let us focus on what happens in the transverse direction X_2 . We take for granted that, owing to the expanding character of the map along X_1 , the attractor is continuous in that direction, which just adds 1 to the dimension found for the transverse part. Following the same idea as for the triadic Cantor set, we can observe that, after one iteration, the length of a segment along X_2 is multiplied by $\kappa' < 1$, which suggests us to take $\varepsilon = (\kappa')^k$ after k iterations. Each application of the map brings about κ reduced copies of the full set, so that we have $\mathcal{N}(\varepsilon) = \kappa^n$. From the formula, we get $d_f = \log(\kappa)/\log(1/\kappa')$ along the contracting direction and thus $1 + \log(\kappa)/\log(1/\kappa')$ for the full attractor displayed in Figure 4.17 (middle part). With $\kappa = 2$ and $\kappa' = \alpha/\kappa$ with $\alpha = 2/3$, this yields $d_f \approx 1.63$.

As an exercise one can look at the aspect of dissipative generalized baker maps with definitions more complex than that illustrated in Figure 4.17, *e.g.* with $\kappa > 2$ and different values of α for different pieces, and then try to determine the dimension of the corresponding (transverse) Cantor sets, which might be less simple than it seems.

4.4 Empirical Approach of Chaotic Systems

Let us consider a chaotic regime observed in a given experiment, *e.g.* in convection. The need of an empirical approach becomes obvious when it appears impossible from a practical point of view to get an *ab initio* understanding of its nature. Most often, even something as qualitative as the type of transition scenario that develops under specific conditions cannot be predicted. For example, in Chapter 3, §3.2.3, we have seen that not only the physical properties of the fluid matters, but the experimental configuration and, in case of attractor coexistence, the history of the experiment also play a role in the transition (though the system, when engaged in a given scenario, follows all its steps at a quantitative level).

Sufficiently far from the threshold of the primary instability, a multiplicity of different possible permanent regimes can be reached by following specific experimental procedures. The effective phase space is thus already very complicated and poorly understood, even when confinement effects select a small number of driving modes. It is therefore fully justified to spend some time to seek a representation of the dynamics in some *reconstruction space* obtained from the experimental records, a space in which the evolution can be described, the amount of chaos can be measured and, hopefully, techniques of control can be developed.

The output of experiments, either in the lab or using a computer, generally presents itself in the form of *time series* of some observable, *i.e.* a series of numerical values taken by some function $W = \mathcal{W}(\mathbf{X})$ of the system's state $\mathbf{X} = (X_1, \dots, X_d)$ in its phase space \mathbb{X} with dimension d .¹⁴ Let us assume a regularly sampled time series:

$$\{W_k, k = 0, 1, \dots\}, \quad \text{with} \quad W_k = \mathcal{W}(\mathbf{X}(t_k)), \quad t_k = k\tau,$$

where τ is the inverse of the sampling frequency.

Just having a look at the plotted time series is a step that should never be skipped since this gives one valuable information on the recurrent or intermittent character of the signal. But clearly more objective analyses are required, especially when the system has reached some sort of attractor, *i.e.* a permanent regime characterized by statistically stationary signals, with distributions that do not change significantly as times goes on, and for

¹⁴For systems evolving in space, the output may also be pictures. This opens the vast field of image processing, basically extending to two-dimensional quasi-continuous arrays the viewpoint of one-dimensional, discrete scalar series on which we focus here exclusively.

which finite-length series are typical of the dynamics, provided that they are not too short (*i.e.* correspond to several turns around the attractor).

The first operations to perform on a time series of length K , $\{W_0, W_1, \dots, W_{K-1}\}$, are of course to compute its average:

$$\overline{W} = \frac{1}{K} \sum_{k=0}^{K-1} W_k,$$

and its variance:¹⁵

$$\sigma_W^2 = \frac{1}{K} \sum_{k=0}^{K-1} (W_k - \overline{W})^2,$$

and then to rescale it by making the changes:

$$\frac{(W_k - \overline{W})}{\sigma_W} \mapsto W_k, \quad k = 0, 1, \dots, K-1.$$

For simplicity, we assume in the following that this preprocessing has been performed, *i.e.* that we work with a signal supposed to be stationary, with zero mean and unit variance.

In a second instance, one usually considers the autocorrelation of the signal defined as:

$$C(\Delta t) = \lim_{T \rightarrow \infty} \frac{1}{T} \int_0^T W(t)W(t + \Delta t) dt. \quad (4.41)$$

In the case of a finite series of discrete records, we get:

$$C(\kappa) = \frac{1}{K - \kappa} \sum_{k=0}^{K-\kappa-1} W_k W_{k+\kappa}, \quad (4.42)$$

but when the series is very long and as long as the shifts κ are small enough ($\kappa \ll K$), any difference with the result of the discrete evaluation of the integral (4.41) for $\Delta t = \kappa \tau$ is not perceptible.

The autocorrelation is the simplest device to identify periodicities in the signal. It is usually not computed from its definition but rather through Fourier transforms. The next section thus begins with a brief reminder about them and continues by introducing the Hilbert transform, a useful tool to perform the demodulation of periodic signals with superimposed slow amplitude and phase variations.

¹⁵The “unbiased” variance should be defined by dividing with $K-1$ instead of K but we are always interested in K large so that this makes no difference.

4.4.1 Standard analysis by means of Fourier transform

On general grounds the direct Fourier transform is defined by:

$$\bar{f}(\omega) = \frac{1}{2\pi} \int_{-\infty}^{+\infty} f(t) \exp(-i\omega t) dt$$

and the inverse transform by:

$$f(t) = \int_{-\infty}^{+\infty} \bar{f}(\omega) \exp(i\omega t) d\omega.$$

The Fourier transform of the autocorrelation function then reads:

$$S(\omega) = \frac{1}{2\pi} \int_{-\infty}^{\infty} C(\tau) \exp(-i\omega\tau) d\tau$$

and a straightforward computation shows that

$$S(\omega) = |\bar{W}(\omega)|^2,$$

where $\bar{W}(\omega)$ is the Fourier transform of $W(t)$. $S(\omega)$ is called the *Fourier spectrum* of the signal.¹⁶

Direct inspection of the signal sometimes suggests that one has to deal with a periodic process that is modulated in amplitude and/or phase. An elegant way to perform the *demodulation* consists in constructing a complex signal $Z(t)$, whose real part is the primitive signal $W(t)$ and whose imaginary part is constructed so as to make a $\pi/2$ phase angle with it. This is easily understood from the consideration of a strictly periodic signal: let $W(t) = A \cos(\omega t)$, the signal at $\pi/2$ is then $A \cos(\omega t - \pi/2) = A \sin(\omega t)$, so that $Z(t) = A \exp(i\varphi(t))$, with amplitude $A = |Z|$ and phase φ , such that $d\varphi/dt = \omega$ is the angular frequency.

In the general case, the instantaneous amplitude of the modulated signal is then given by the modulus of Z and its instantaneous period is derived from its argument by differentiating it with respect to time, provided that one knows how to obtain the signal at $\pi/2$. This is done from the Fourier transform of $W(t)$, by copying the case of the periodic signal taken as an example above, frequency by frequency. Starting with:

$$W(t) = \int_{-\infty}^{+\infty} \bar{W}(\omega) \exp(i\omega t) d\omega, \quad (4.43)$$

¹⁶This result is called the Wiener-Kintchine theorem. The derivation uses a few tricks, among which the fact that the Fourier transform of a constant $f \equiv 1$ is a Dirac distribution $\delta_D(\omega)$.

and setting:¹⁷

$$\tilde{W}(\omega) = \frac{1}{2}[A(\omega) + iB(\omega)] = \tilde{W}(-\omega)^*, \quad (4.44)$$

one can observe that $A(\omega)$ and $B(\omega)$ are even and odd functions of ω , respectively. In full generality one gets $B(0) = 0$ and, further also $A(0) = 0$, since $W(t)$ is assumed to have zero mean. Expression (4.43) can then be rewritten as:

$$W(t) = \int_0^{+\infty} [A(\omega) \cos(\omega t) - B(\omega) \sin(\omega t)] d\omega,$$

which allows one to get the imaginary part, here denoted W' :

$$W'(t) = \int_0^{+\infty} [A(\omega) \cos(\omega t - \pi/2) - B(\omega) \sin(\omega t - \pi/2)] d\omega,$$

which more simply reads:

$$W'(t) = \int_0^{+\infty} [B(\omega) \cos(\omega t) + A(\omega) \sin(\omega t)] d\omega.$$

By definition of $Z = W + iW'$, one then obtains:

$$Z(t) = \int_0^{+\infty} \exp(i\omega t) [A(\omega) + iB(\omega)] d\omega, \quad (4.45)$$

which involves a sum over the positive angular frequencies (the so-called ‘analytical signal’). Comparing (4.45) and (4.43, 4.44), one obtains the Fourier transform $\tilde{Z}(\omega)$ by setting to zero all components of the Fourier transform of W corresponding to negative angular frequencies and by doubling all the others. The analytic signal $Z(t)$ itself is then recovered by computing the inverse transform of \tilde{Z} . Mathematically W and W' are Hilbert transform of each other¹⁸ hence the expression ‘Hilbert transform demodulation’ (the full procedure is implemented by `hilbert.m` in the MATLAB software).

4.4.2 Reconstruction by the method of delays

Let us now take a point of view more in line with the theory of dynamical systems. A difficulty arises immediately from the fact no specific assumption can be made, except that a deterministic framework is relevant, so that

¹⁷The complex conjugation property arises from the fact that the observable W is supposed to be a real function of \mathbf{X} .

¹⁸Formally, $W'(\omega) = -(1/\pi) \mathcal{P} \int_{-\infty}^{\infty} [\tilde{W}(\omega')/(\omega - \omega')] d\omega'$, where \mathcal{P} denote the Cauchy principal part of the integral.

one can just write formally $\dot{\mathbf{X}} = \mathcal{F}(\mathbf{X})$ for unspecified states living in some space \mathbf{X} . In particular, the nature and the dimension d_{eff} of the manifold supporting the dynamics,¹⁹ and the explicit relation between states and the observable $W = \mathcal{W}(\mathbf{X})$ are not known *a priori*.

Practically all reconstruction techniques derive from the *method of delays* mathematically formalized by Takens in 1981,²⁰ which is numerically more robust than a previous approach based on the evaluation of successive time derivatives of the experimental signal in terms of finite differences.²¹

Let us illustrate the reconstruction approach using a discrete-time system for simplicity. At the beginning we assume that

$$\mathbf{X}_{k+1} = \mathcal{F}(\mathbf{X}_k)$$

and that the time series of some scalar observable \mathcal{W} is available (the method is, at least conceptually, easy to extend to the case of several observables). Reconstructing the dynamics means determining an empirical relation between the \mathbf{X}_k in their phase space only from the knowledge of the W_k , $k = 0, 1, \dots$

A single measure $W_0 = \mathcal{W}(\mathbf{X}_0)$ is not sufficient to determine the state \mathbf{X}_0 since we surely need more than one coordinate to define it. But we assume that the next value W_1 corresponds to a point \mathbf{X}_1 that evolves from \mathbf{X}_0 under the map \mathcal{F} , unknown but existing. The second measurement thus adds a piece of information about the coordinates of \mathbf{X}_0 through $W_1 = \mathcal{W}(\mathbf{X}_1) = \mathcal{W}(\mathcal{F}(\mathbf{X}_0))$. The third one, $W_2 = \mathcal{W}(\mathbf{X}_2) = \mathcal{W}(\mathcal{F}(\mathbf{X}_1)) = \mathcal{W}(\mathcal{F}(\mathcal{F}(\mathbf{X}_0)))$ adds another piece, *etc.* In principle, a sufficiently long series of d_{test} successive measurements, $\{W_0, \dots, W_{d_{\text{test}}-1}\}$, should serve us to specify \mathbf{X}_0 . In the same way, $\{W_1, \dots, W_{d_{\text{test}}}\}$ would do so for \mathbf{X}_1 , *etc.* Eventually a whole trajectory would then be reconstructed from the series of vectors in $\mathbb{R}^{d_{\text{test}}}$:

$$\mathbf{V}_k = [W_k; \dots; W_{k+d_{\text{test}}-1}] .$$

The concrete implementation of the method is by increasing the dimension of the reconstruction space until a consistent quantitative assessment of the observations can be given. In practice, the problem can be reformu-

¹⁹The dimension of the physical system itself is usually infinite; think of continuous media.

²⁰F. Takens, "Detecting strange attractors in turbulence," Lect. Notes Math. **898** (1981) 366–381.

²¹N.H. Packard, J.P. Crutchfield, J.P., J.D. Farmer, R.S. Shaw, "Geometry from a time series," Phys. Rev. Lett. **45** (1980) 712–716.

lated in terms of the *reliability* of the reconstruction. The space of vectors \mathbf{V}_k has to be in correspondence with the region of phase space visited by the system when the permanent regime is reached. Whereas we can accept redundancy, *i.e.* a dimension d_{test} that is too large, we must not lose useful dynamical information. In mathematical terms the representation of the system must be *injective*, so that different states have different reconstructions:

$$\mathbf{X}_k \neq \mathbf{X}_{k'} \Rightarrow \mathbf{V}_k \neq \mathbf{V}_{k'}. \quad (4.46)$$

What was defined as a tentative number of component d_{test} is thus more mathematically understood as the dimension of the space in which the effective phase space can be *embedded* by means of some injective map. To stick with this abstract point of view more closely, we now define d_{test} as the *embedding dimension*, denote it d_e , and thus specify states in the embedding space as:

$$\mathbf{V}_k = [W_k; \dots; W_{k+d_e-1}], \quad (4.47)$$

Takens' method of delays is sketched in Figure 4.19. His theorem states that the \mathbf{V}_k defined above, where the observable W is defined by a differentiable functional on phase space \mathcal{W} , achieve a reliable reconstruction provided that the dimension d_e is large enough: $d_e \geq 2d_{\text{eff}} + 1$, where d_{eff} is the topological dimension of the manifold supporting the effective dynamics.

This theorem can be understood as an extension to the present context of Whitney's theorem that states that a compact d -dimensional differentiable manifold \mathbb{M} can be embedded in an Euclidean space \mathbb{R}^{2d+1} . As an illus-

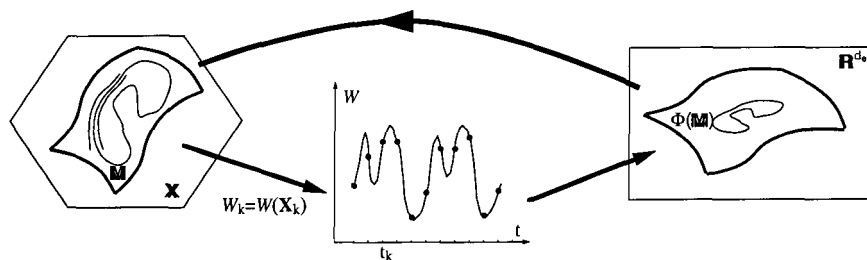


Fig. 4.19 Illustration of Takens' theorem. \mathbb{M} is the manifold in the space \mathbb{X} over which the effective dynamics takes place. Coordinates of points representing the system in \mathbb{R}^{d_e} are obtained from the series of measurements W_k through (4.47).

tration of the latter, one can consider a loop (dimension 1) that would be projected on a plane as the figure eight. In order to resolve its structure, and in particular to check that the intersection is a fake, one must be able to look at the loop from another side, *i.e.* to stand in a $2 \times 1 + 1 = 3$ dimensional space.

In fact the reconstruction proposed by Takens is more general than that proposed by (4.47) since the V_k can be any series of d_e measurements, $[W_k; W_{k+\kappa_1}; \dots; W_{k+\kappa_{d_e-1}}]$, and nothing forbids it to take irregularly distributed intervals κ_q . It is however natural to take κ_q as the successive multiples of some basic κ , *i.e.* $\kappa_q = q\kappa$, $q = 1, 2, \dots, d_e - 1$. When the signal is obtained from the time sampling of a continuous-time system with period τ this corresponds to a sub-sampling at period $\kappa\tau$.

The mathematical viewpoint developed so far is apparently strong. However our enthusiasm must be somewhat tempered and a pragmatic perspective has to be taken, for it is not clear that the physical systems we are interested in fulfill the theoretical conditions underlying the theorem, and first of all that the d_{eff} -dimensional manifold over which the dynamics takes place is sufficiently smooth. As it is usually the case for chaotic nonlinear systems, the attractor has a fractal dimension $d_f \geq d_{\text{eff}}$ and, following Mañé (1981), one can replace d_{eff} by d_f in the inequality for d_e . This still does not lead to any concrete estimate, in part because measurements are always polluted by “noise” that comes and hinders the reconstruction. Strategies have thus been developed to get around these difficulties and determine more or less optimally the two basic ingredients of any reconstruction: the base delay κ and the embedding dimension d_e . This is what we now briefly discuss, inviting the interested reader to consult, *e.g.* [Abarbanel (1996); Kanz and Schreiber (1997); Weigend and Gershenfeld (1993)] for more detailed approaches.

4.4.3 Sampling frequency and embedding dimension

For more specificity we use a synthetic signal obtained by numerical simulation of a noisy limit cycle governed in the complex plane $Z = X + iY$ by a *Langevin equation*

$$\dot{Z} = (1 + i)Z - (1 - i)|Z|^2 Z + \zeta(t),$$

where $\zeta(t)$ is a Gaussian noise. We assume that the trajectories are computed by a second order Runge–Kutta scheme (B.9–B.10) with time step $\delta t = 0.01$. A noise with amplitude 0.05 is added to X and Y at each time

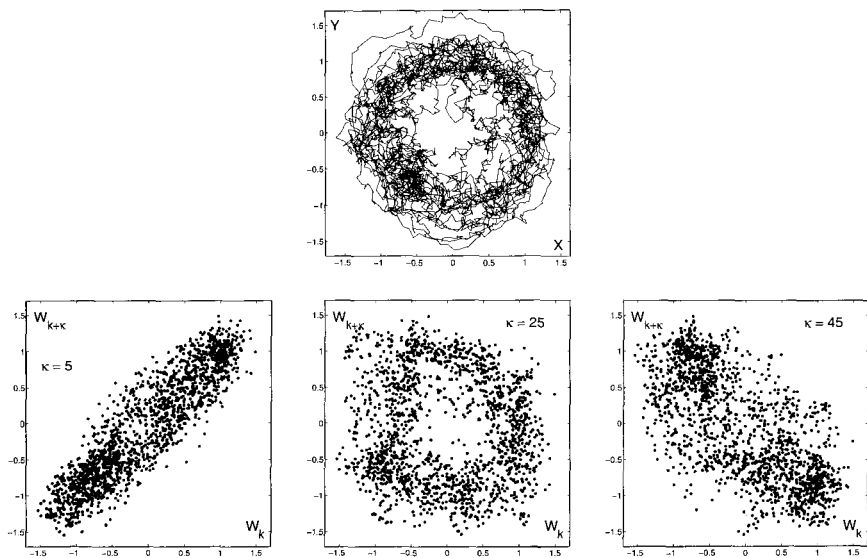


Fig. 4.20 Top: Original noisy periodic signal in its own phase space. Bottom: Reconstruction with sampling time $\tau = 0.03$ and delays $\kappa = 5, 25$ and 45 of observable $W(t) \equiv X(t)$.

step (for the generation of Gaussian noise see [Press *et al.* (1986)]). The trajectory used for this example is displayed in Figure 4.20 (top). The period of the (deterministic) signal is $T = \pi$. The signal $W(t)$ that we take is just the X component of the trajectory and we mimic the sampling process by recording its value every $\tau = 3\delta t$.

The first problem is that of the sampling time, and thus that of κ . An exaggerately high frequency is not an advantage since a huge volume of data is produced, the most part of which is redundant owing to the noise that blurs the information. It is then believed that the delay between two successive records must be sufficient to bring novel information. A practical rule is to take the delay corresponding to the first zero of the autocorrelation as the effective sampling time $\kappa\tau$. For the present (deterministic) sinusoidal signal, $W(t) = \sin(2t)$, the autocorrelation defined through (4.41) is $C(\Delta t) = \cos(2\Delta t)$ and this rule prescribes $\Delta t = \pi/4$, *i.e.* a quarter of a period: two measurements out of phase by such a shift are indeed fully discriminated since one is maximum when the other is zero.

The discrete estimate of the autocorrelation function (4.42) is displayed in the left part of Figure 4.21 where one can observe that the noise adds

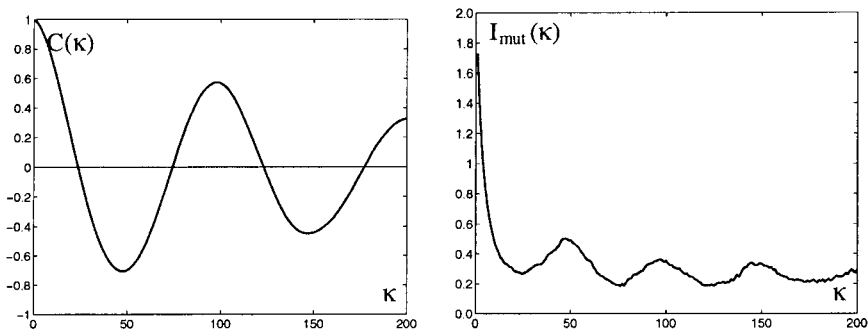


Fig. 4.21 Autocorrelation $C(\kappa)$ and mutual information $I_{\text{mut}}(\kappa)$ of signal W in Figure 4.20 as a function of the delay κ .

a slight damping to the behavior expected for a periodic signal. Applying the rule leads to $\kappa \simeq 25$, which indeed corresponds to a quarter of a period once recalled that $\tau = 3\delta t = 0.03$. Two-dimensional reconstructions in the plane $(W_k, W_{k+\kappa})$ for $\kappa = 5, 25$ and 45 are displayed in Figure 4.20 (bottom row) which shows that the representation with $\kappa = 25$ is the most similar to the original signal, whereas for $\kappa = 5$ and $\kappa = 45$, corresponding to measurements too close in time or practically in phase opposition, the reconstructions align along directions $W_{k+\kappa} = +W_k$ and $W_{k+\kappa} = -W_k$, respectively.

The study of the autocorrelation function, of linear essence, does not always lead to a satisfactory choice of κ . Let us now mention a more general criterion resting on a similar philosophy but with a better nonlinear flavor. This criterion bears on the *mutual information* contained in two records shifted by some time amount when compared to that contained in a single record. Again, stationarity of the signal is assumed. First the probability distribution $\mathcal{P}(W)$ of $W_k = W$ is obtained by an appropriate normalization of the histogram of the values of W_k . Next, the joint probability $\mathcal{P}_\kappa(W', W'')$ is determined in the same way but for couples $(W_k = W'; W_{k+\kappa} = W'')$, with $\kappa = 1, 2, \dots$. From these, the *mutual information* is defined as:

$$I_{\text{mut}}(\kappa) = \sum_{W', W''} \mathcal{P}_\kappa(W', W'') \ln \left(\frac{\mathcal{P}_\kappa(W', W'')}{\mathcal{P}(W')\mathcal{P}(W'')} \right). \quad (4.48)$$

This quantity is a measure of the redundancy in the signal: when κ is small, points in phase space are highly correlated so that learning about

$W_{k+\kappa}$ when W_k is known does not bring much novel information; by contrast when $\kappa \gg 1$, the points become uncorrelated and $\mathcal{P}_\kappa(W_k, W_{k+\kappa})$ is essentially $\mathcal{P}(W_k)\mathcal{P}(W_{k+\kappa})$, so that the mutual information is nearly zero, the information gained is the same as from independent drawings W_k and $W_{k+\kappa}$ using $\mathcal{P}(W)$. As can be seen from the right part of Figure 4.21 that displays the graph of $I_{\text{mut}}(\kappa)$ obtained by applying (4.48) to our signal, the mutual information does not decrease monotonically but in general presents a first minimum at some intermediate κ that defines an optimal value κ_{opt} corresponding to a minimum of the redundancy, before ultimately decaying owing to statistical decorrelation: taking simultaneously W_k and $W_{k+\kappa_{\text{opt}}}$ should thus give the best information about the dynamical evolution. Here, without surprise κ_{opt} is the same as that given by the previous rule, but more generally this is not the case.

It should be noted that, when no clear minimum of $I_{\text{mut}}(\kappa)$ is obtained, this can mean either the presence of a very large noise, or that the observable has been under-sampled, or that too many degrees of freedom are involved, all cases where methods of the theory of low dimensional deterministic dynamical systems are of little help.

Once the parameter κ has been determined optimally, one can re-sample the time series with the new step and discard redundant information contained in the intermediate values that are too closely correlated to the retained ones. In fact, the κ parallel time series obtained by changing the phase of the reconstruction modulo κ are not independent but yield κ equivalent reconstructions of one and the same trajectory. Comparing these reconstructions may serve to appreciate the amount of noise quantitatively.

Renumbering the time series, we can assume $\kappa = 1$ and focus on our second problem: finding the most appropriate embedding dimension d_e .

Keeping in mind that we want to obtain an injective representation, we reverse the implication (4.46), now stated:

$$\mathbf{V}_k = \mathbf{V}_{k'} \quad \Rightarrow \quad \mathbf{X}_k = \mathbf{X}_{k'},$$

which suggests to analyze the reliability of the state identification (r.h.s.) from comparisons of different reconstructions (l.h.s) especially in spaces with different dimensions: neighbors in some space are “true neighbors” if they remain so for all reconstructions. This property can be checked by increasing d_e , i.e. enlarging the width of the window dragged on the data.

The *method of false neighbors* is an efficient strategy to decide when to stop adding coordinates. Consider a trial dimension d' , i.e. $[W_k; W_{k+1}; \dots; W_{k+d'-1}]$ and the $(d' + 1)$ -dimensional reconstruction ob-

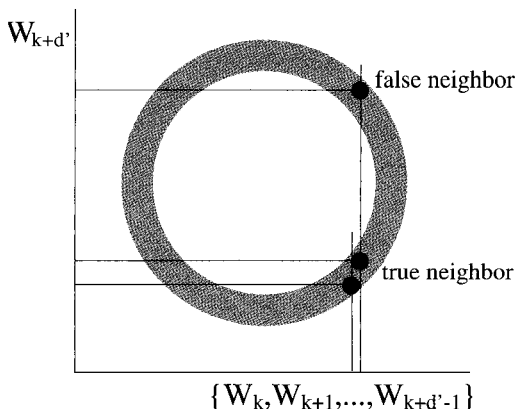


Fig. 4.22 Comparison of the reconstruction in a d' -dimensional space featured by the horizontal axis (coordinates $\{W_k; \dots; W_{k+d'-1}\}$), and a reconstruction in the $(d' + 1)$ -dimensional space obtained by adding coordinate $W_{k+d'}$.

tained by adding a component $W_{k+d'}$. Choose a distance in reconstruction space and a criterion to decide which is neighbor and which is not (depending on the noise amplitude). Next determine the number of false neighbors, *i.e.* the number of pairs of points that were neighbors in d' dimensions and are no longer neighbors in $d' + 1$ dimension, as illustrated in Figure 4.22. Then increase d' up to the point when the fraction of false neighbors decreases significantly and choose that value as optimal embedding dimension.

The Euclidean distance derived from the L^2 norm is usually not a convenient choice for neighborhood evaluations, since it requires a lot of computations. By contrast, the distance derived from the L^∞ -norm, *i.e.*

$$\text{dist}(\mathbf{V}^{(1)}, \mathbf{V}^{(2)}) = \sup_k |V_k^{(1)} - V_k^{(2)}|.$$

only requires comparisons and is most economical.

Choosing the embedding dimension as given by the false-neighbor method should appropriately unfold the structure of the attractor. The final presentation of the result can be improved by changing from the canonical basis in the reconstruction space to a basis correlated to the data in the least-square sense.²² The method known as *proper orthogonal decomposi-*

²²(a) The idea was introduced by D.S. Broomhead and G.P. King, "Extracting qualitative dynamics from experimental data," *Physica D* **20** (1986) 217–236. (b) For a concrete implementation, see R. Vautard, P. Yiou, and M. Ghil, "Singular spectrum analysis: a toolkit for short, noisy chaotic signals," *Physica D* **58** (1992) 95–126.

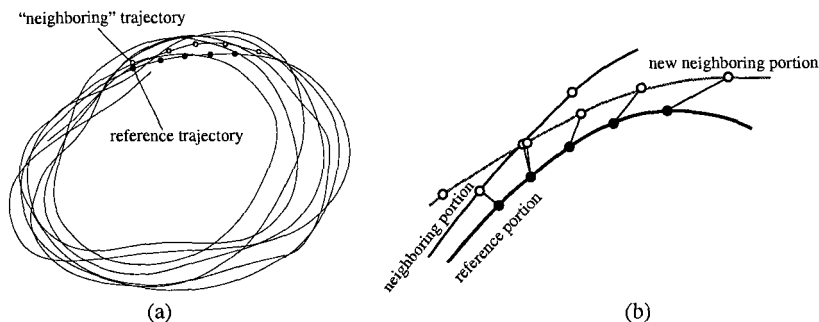


Fig. 4.23 Empirical determination of the largest Lyapunov exponent of a system in its reconstructed phase space. (a) Reconstructed attractor. (b) Rescaling of the distance between the reference portion of trajectory and its neighbor.

tion or *singular value decomposition* is implemented in numerical softwares such as MATLAB and is also used in the field of pattern recognition, which may be of interest in the analysis of space-time chaos to be introduced in Chapter 5.

4.4.4 Application

From a d_e -dimensional reconstruction one can next extract quantitative information of the system, and in particular the amount of chaos present, using quantities such as Lyapunov exponents or fractal dimensions of the attractor.

By contrast with the theoretical approach, in which the expression of the dynamical system is known, here we have just a (very long) time series of some observable at given control parameter. The attractor is then first reconstructed by the method of delays from this time series, Figure 4.23(a), and we must assume at this stage that the permanent regime is reached and that the system explores its attractor repeatedly and satisfactorily in a statistical sense. If this is the case, when the system comes in a given region of phase space, it never comes exactly at the same place but in some neighborhood. Taking a portion of the trajectory as a reference, the vector field in its neighborhood can be estimated from the set of trajectory pieces followed in close approaches to that reference portion, *e.g.* through a least-square adjustment of the coefficients of the local Jacobian matrix. This is in general a hard matter. A quantity that can however be determined more easily

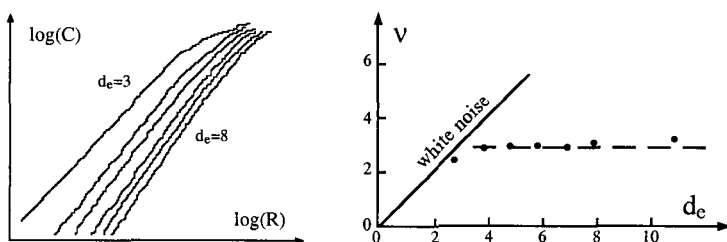


Fig. 4.24 Determination of the correlation dimension in a convection experiment. Left: Distribution of distances in phase space for several embedding dimensions. Right: Variation of the slope at small R as d_e is increased. Exponent ν is seen to saturate at 2.8 which is the correlation dimension of the considered attractor. When d_e is too small, trajectories fill the reconstruction space homogeneously, as if the signal was a white noise, hence the corresponding line $\nu = d_e$. After Malraison *et al.*, Note 25.

is the largest Lyapunov exponent. The procedure used in early attempts²³ reflects particularly clearly its nature as an average trajectory divergence rate: since Lyapunov exponents are quantities relative to the tangent evolution, the distance between pieces of trajectories serving to compute the divergence rate must remain small enough; when following the reference trajectory, one is therefore obliged to look for pieces of trajectories as close as possible to the current point, in the direction of fastest divergence, as suggested in Figure 4.23(b).

A quantity that can serve to characterize the fractal properties of strange attractors is the *correlation dimension* introduced by Grassberger and Procaccia.²⁴ It is extracted from the distribution of distances between pairs of points on the reconstructed attractor $\Delta(\mathbf{V}_i, \mathbf{V}_j)$, obtained by computing

$$C(R) = \lim_{N \rightarrow \infty} \frac{1}{N^2} \sum_{\{\mathbf{x}_i, \mathbf{x}_j\}} \Upsilon(R - \Delta(\mathbf{V}_i, \mathbf{V}_j)), \quad (4.49)$$

where $\Upsilon = 0$ for $u < 0$, and $\Upsilon(u) = 1$ for $u > 0$ (Heaviside distribution). Provided that the statistic is sufficient, this quantity measures the number of points in volume elements of radius R around each point, roughly speaking its mass, as it varies with R . For a compact d -dimensional object, one would have $C(R) \sim R^d$ as $R \rightarrow 0$. The correlation dimension is thus

²³A. Wolf, J.B. Swift, H.L. Swinney, J.A. Vastano, "Determining Lyapunov exponents from a time series," *Physica D* **16** (1985) 285–317.

²⁴P. Grassberger, I. Procaccia, "Measuring the strangeness of strange attractors," *Physica D* **9** (1983) 189–208.

defined as

$$\nu = \lim_{R \rightarrow 0} \frac{\log(C(R))}{\log(R)}. \quad (4.50)$$

The way it is defined makes exponent ν similar to d_f . As such, it gives an easily determined measure of the fractal character of the attractor from the statistics of a long time record in the embedding space.

This approach has been developed many times. The example given here is the first application to a concrete convection experiment in confined geometry, by Malraison *et al.*²⁵ It is seen in Figure 4.24 (left) that the correlation integral (4.49) plotted in log-log scale as a function of R indeed display a linear part at small R from which an exponent ν can be derived. At the time of the experiment, the determination of the optimal embedding dimension was made by just increasing d_e progressively.

If the embedding dimension is chosen too small, one observes that ν is close to d_e which is easily understood from the fact that the reconstruction does not contain enough information to evidence the deterministic character of the dynamics. Points fill the V -space homogeneously as a random signal would do. On the contrary, if upon increasing d_e , it happens that ν saturates at some finite value, as here, it is a good indication that some deterministic dynamics is at work producing a low dimensional chaos, see Figure 4.24 (right). If unfortunately, ν continues to increase with d_e , either confinement effects are too weak and the effective signal is not low dimensional, or the noise level is too high.

To conclude this section, let us remark that a reliable quantitative determination of the amount of chaos requires a lot of data but that useful information can anyway be obtained from the reconstruction technique, *e.g.* to attempt controlling chaos.²⁶ Software packages are available for an automatic treatment of experimental data, *e.g.* Note 22(b).

²⁵B. Malraison, P. Atten, P. Bergé, M. Dubois, "Dimension d'attracteurs étranges: une détermination expérimentale en régime chaotique de deux systèmes convectifs," C.R. Acad. Sc. Paris **297** Série II (1983) 209–214.

²⁶Chaos control and its applications have received considerable attention in the 1990s. See, *e.g.* T. Shinbrot *et al.*, "Using small perturbations to control chaos," Nature **363** (1993) 411–417; S. Hayes *et al.*, "Communicating with chaos," Phys. Rev. Lett. **70** (1993) 3031; for another approach, see K. Pyragas, "Continuous control of chaos by self-controlling feedback," Phys. Lett. A **170** (1992) 421–428, and W. Just, *et al.*, "Mechanism of time-delayed feedback control," Phys. Rev. Lett. **78** 203–206. A more complete presentation can be found in [Schuster (1999)].

4.5 Conclusion

As a whole, one can say that the problem of the transition to turbulence in strongly confined systems is, at least at a conceptual level but also most often at a practical quantitative level, well understood in terms of temporal chaos and a small set of universal scenarios.

This framework is, by construction, that of discrete systems introduced in Chapter 2. It can also legitimately be applied to continuous systems in case of strong confinement effects, by virtue of the distinction between driving and enslaved modes and the adiabatic elimination of the latter, thus offering a vast field where a detailed comparison of theory, tools and concepts, and laboratory or numerical experiments is meaningful.

The next chapter is devoted to the study of the case when confinement effects are no longer sufficiently strong to restrict the effective dynamics to the interaction of such a small number of discrete modes.

4.6 Exercises

4.6.1 *Homogeneous instability in a confined context*

Consider a spatially extended system governed by

$$\partial_t v = rv + \partial_{xx} v - v^3.$$

- 1) Linearized problem: determine the growth rate of Fourier modes $\propto \exp(ikx)$ with infinitesimal amplitude in a laterally unbounded system and obtain the marginal stability condition of the trivial solution $v \equiv 0$.
- 2) Adding boundary conditions $v(x) = 0$ at both ends of the interval $[0, \pi]$, check that one can take eigenmodes in the form $X_n = \sin(nx)$ and determine their growth rate as a function of n .
- 3) Find the condition on r such that only the first mode is excited, while others remain strongly stable. When this is the case, assuming $v(x, t) = A_1(t)X_1(x)$, determine the equation governing A_1 within a first-harmonic approximation. Show that the system experiences a supercritical fork bifurcation.
- 4) The cubic nonlinearity generates modes X_n , $n > 1$. Find the equation governing A_3 , its order of magnitude at steady state when $r \ll 1$, and justify the approximation made.

4.6.2 Cellular instability in a confined context

Go back to model (3.39) and complete it by a nonlinear advection-like term to get:

$$\partial_t v + v \partial_x v = r v - (\partial_{xx} + 1)^2 v. \quad (4.51)$$

Then consider a confined system with boundary conditions $v = \partial_{xx} v = 0$ at $x = 0$ and $x = \ell$. Check that modes in the form $\sin(k_n x)$ are appropriate and insert expansion:

$$v(x, t) = \sum_{n=1}^{\infty} A_n(t) \sin(k_n x), \quad k_n = n\pi/\ell, \quad (4.52)$$

in (4.51). Further separate the different harmonics and obtain the set of ordinary differential equations governing the amplitudes A_n . Write down explicitly the equations for A_1 , A_2 and A_3 when $\ell = \pi$ for $r \ll 1$. Show that in this limit A_2 , A_3, \dots are enslaved to A_1 . Propose a coherent truncation of the system above some order $N \geq 2$ fixed in advance.

When truncated at order 2 the system reads:

$$\dot{A}_1 = r A_1 + \frac{1}{2} A_1 A_2 \quad (4.53)$$

$$\dot{A}_2 = -9 A_2 - \frac{1}{2} A_1^2 \quad (4.54)$$

Sketch its phase portrait in the reduced phase space (A_1, A_2) . Determine the effective dynamics of A_1 obtained by adiabatic elimination of A_2 and the nature of the bifurcation as r increase from negative to positive values.

4.6.3 Landau model of bifurcation for one real mode

Let A be a real variable governed by a first-order differential equation:

$$\dot{A} = \mathcal{F}(A). \quad (4.55)$$

In Chapter 2, §2.1.3 it was shown that this equation can be written in gradient form $\dot{A} = -\partial \mathcal{G} / \partial A$, so that \mathcal{G} decreases as A evolves. Consider now the neighborhood of a time-independent base state A_0 such that \mathcal{G} is stationary, $F(A_0) = -\partial_A \mathcal{G}(A_0) \equiv 0$.

1) Rewrite the equation governing the dynamics of a “perturbation” A'

defined by $A = A_0 + A'$ as a Taylor expansion

$$\dot{A}' = \sum_n a_n (A')^n, \quad (4.56)$$

express the linear stability condition for A_0 in terms of the derivatives of \mathcal{F} at A_0 and interpret this condition in terms of \mathcal{G} . By appropriate notational changes and rescalings we assume that $A_0 = 0$ and that the linear growth-rate σ of A is simply given by $\sigma = r$, which define $r = 0$ as the bifurcation threshold. Equation (4.56) then reads

$$\dot{A} = rA + \sum_{n \geq 2} a_n A^n. \quad (4.57)$$

Assuming that the system can be truncated beyond some order N , using either \mathcal{F} or \mathcal{G} , show that the dynamics described by (4.57) is meaningful in the sense that A remains finite for all times, provided that N is an odd integer and a_N is negative. (When N is even, the model is only locally valid and should be completed by terms of higher degree to acquire a more global validity). Find the conditions fulfilled by coefficients a_n in (4.57) when the system is invariant through the symmetry $A \mapsto -A$.

2) When $N = 2$, consider the systems:

$$\dot{A} = r_0 - A^2 \quad (4.58)$$

and

$$\dot{A} = r_1 A - A^2. \quad (4.59)$$

Draw the graphs giving their fixed points A_* (*bifurcation diagrams*) against the control parameters r_0 or r_1 , and indicate their stability properties, using solid (dashed) lines for stable (unstable) fixed points. Justify the terms *saddle-node* and *trans-critical* for these two bifurcations.

3) Same exercise when $N = 3$ with systems:

$$\dot{A} = rA - A^3 - H, \quad (4.60)$$

producing the imperfect bifurcation (Fig. 4.4, p. 127) and

$$\dot{A} = rA - A^2 - A^3. \quad (4.61)$$

accounting for a perfect bifurcation perturbed by a breaking of the symmetry $A \mapsto -A$. Observe that, in both cases, elements of the case $N = 2$ are recovered locally in the plane (r, A_*) .

6) Consider the case $N = 5$ with symmetry $A \mapsto -A$:

$$\dot{A} = rA + aA^3 - A^5, \quad (4.62)$$

coefficient a being positive or negative.

a) Determine the position of the fixed points at given (r, a) .

b) When a is positive, show that the bifurcation at $r = 0$ is subcritical and that the system experiences hysteresis cycles as r is varied. Draw the bifurcation diagram and observe the presence of situations already studied for smaller maximum degree N . Determine the shape of potential \mathcal{G} corresponding to the different cases.

c) consider briefly (4.62) with $a < 0$ and identify the different nonlinear regimes according to which of the nonlinear terms controls the position of the fixed point.

Remark. Equation (4.58) is said to be the generic unfolding of the quadratic nonlinearity. It is indeed more general than (4.59) that additionally supposes the persistence of the fixed point at $A = 0$ [incidentally, this is also the case of (4.57)]. On more general grounds, one can always find the translation $A \mapsto A + \alpha$ that suppresses the coefficient a_{N-1} , and rescale A so that $a_N = \pm 1$. The generic unfolding of $\dot{A} = \pm A^N$ then reads:

$$\dot{A} = r_0 + r_1 A + \cdots + r_{N-2} A^{N-2} \pm A^N,$$

where the *unfolding parameters* r_n are perturbations, *i.e.* must remain small when compared to the absolute value of the coefficient of the highest degree term (± 1 after rescaling). This system may have no fixed points, as seen above for $N = 2$ with (4.58) when $r_0 < 0$.

4.6.4 Variation on the theme of Exercise 4.6.3

Consider the system

$$\dot{A} = \mathcal{F}_r(A) = -A/r + 2A^2 - A^3, \quad r > 0.$$

1) Determine explicitly the potential $\mathcal{G}_r(A)$ from which it derives, up to an arbitrary constant that will be taken as zero.

2) Find the fixed points as functions of the control parameter r . Show that a pair of fixed points appear through a saddle-node bifurcation at some value of r to be determined. Study the stability of the different fixed points and compute the value of the corresponding potentials.

3) Find the asymptotic behavior of the non-trivial fixed points as $r \rightarrow +\infty$ and draw the bifurcation diagram.

4) In the Landau theory of phase transition \mathcal{G} would be a good model of free energy for a first-order transition, *e.g.* the liquid-gas transition. Compute the value r_M of parameter r corresponding to the Maxwell plateau at which the free energies of the two competing stable states are equal. Draw the graph of \mathcal{G}_r for $r < r_M$, $r = r_M$, and $r > r_M$.

4.6.5 Excitable system

Consider a dynamical system in the form

$$\dot{X} = F_Y(X) = X - X^3 - Y, \quad (4.63)$$

where Y is, for the moment, a parameter.

Determine the fixed points of (4.63), their number and nature (stable or unstable) as Y is varied. Determine the potential from which this equation derives (see Exercise 4.6.3, above).

Suppose now that Y is a dynamical variable of its own, governed by

$$\dot{Y} = \epsilon(X - r), \quad (4.64)$$

where $0 < \epsilon$ is a constant and r the control parameter.

Determine the character of the fixed point of system (4.63, 4.64) as a function of r , assuming that $1 - 3r^2 \neq 0$ and $\epsilon \ll |1 - 3r^2|$.

Interpret the phase portrait of the system in the two cases $|r| < 1/\sqrt{3}$ and $|r| > 1/\sqrt{3}$. In the first case, explain the shape of the relaxation oscillations observed after damping of the transient. See Fig. 4.25.

In the second case, the system is said to describe an excitable medium such that, for initial conditions $X > r$, the relaxation of the system towards its fixed point occurs after a large pulse. [In a reaction-diffusion system where the reaction part is accounted for by (4.63, 4.64), the system develops fronts separating excited regions from relaxed one].

4.6.6 Stability and attractors of a two-dimensional system

Consider the system

$$\dot{X} = -aX + Y + XY, \quad (4.65)$$

$$\dot{Y} = -bY - X^2, \quad (4.66)$$

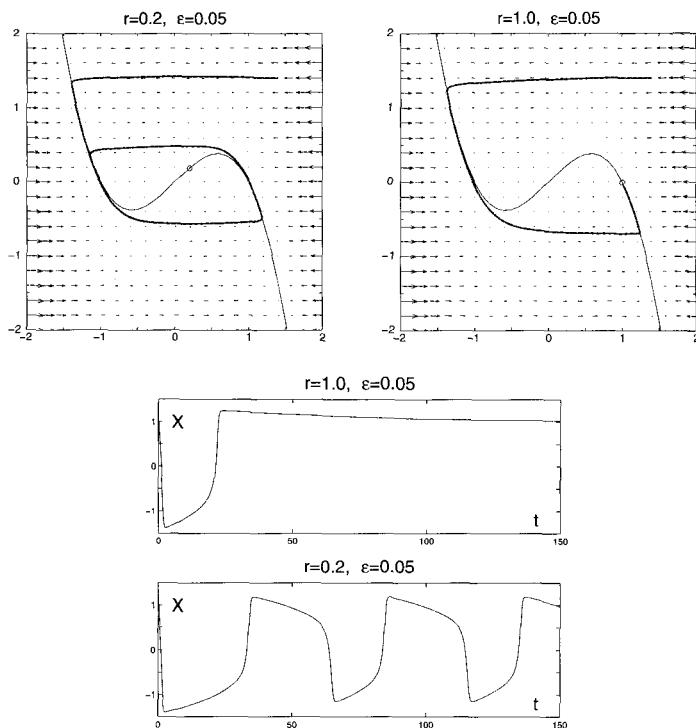


Fig. 4.25 Excitable system. Top: Phase portraits. Bottom: Time series of variable X

where a and b are constants. By computing the eigenvalues and eigenvectors of the system when linearized around the origin $X = Y = 0$, show that it remains locally stable (stable with respect to infinitesimal perturbations) as long as $a > 0$ and $b > 0$. Sketch the phase portrait of the linearized system for $a < b$.

Consider now the system with its nonlinear terms and determine the fixed points as functions of $\Delta = 1 - 4ab$. This quantity will serve as a control parameter in the following. Show that a saddle-node bifurcation takes place when Δ changes its sign. Find the eigenvalues and eigenvectors of the vector field linearized around each non-trivial fixed point.

Sketch the phase portrait of the system for $\Delta < 0$, $\Delta = 0$, and $\Delta > 0$ (take e.g. $b = 1$ and values of a that lead to simple numerical applications, in particular $a = 1/4, 3/16$). Observe that the stable manifold of the unstable fixed point that extrapolates its stable eigendirection is the boundary

between the attraction basins of the two stable fixed points when they exist. Notice that the nonlinearities profoundly modify the aspect of the phase portrait expected from the linear analysis close to the origin. Numerical simulation of (4.65, 4.66) is recommended.²⁷

4.6.7 *Bruzellator*

The system obtained in Exercise 1.5.1 reads

$$\dot{X} = A - (B + 1)X + X^2Y, \quad (4.67)$$

$$\dot{Y} = BX - X^2Y. \quad (4.68)$$

Find its fixed points as functions of parameters A and B and discuss their linear stability properties. Show that the reaction can bifurcate from a time-independent state towards an oscillatory regime beyond some critical value B_c to be determined as a function of A .

Compute the eigenvalues at lowest order in $\varepsilon = B - B_c$. Adapt the first harmonic approximation of Chapter 2, §2.3.1.2, p. 49 to derive the amplitude equation governing the system beyond threshold.

4.6.8 *Locking*

In a permanent regime, an oscillator can be described using a phase variable θ defined modulo 2π and governed by $\dot{\theta} = \omega$ where ω is the angular frequency of the oscillator. Consider two such oscillators weakly but nonlinearly coupled, governed by:

$$\begin{aligned} \dot{\theta}_1 &= \omega_1 - f(\theta_2 - \theta_1), \\ \dot{\theta}_2 &= \omega_2 - f(\theta_1 - \theta_2). \end{aligned}$$

Justify the fact that function f has to be periodic with period 2π . In the following, take $f(\varphi) = \frac{1}{2}K \sin(\varphi)$ and write down the system for $\bar{\theta} = \frac{1}{2}(\theta_1 + \theta_2)$ and $\varphi = \frac{1}{2}(\theta_1 - \theta_2)$ (define $\delta\omega = \frac{1}{2}(\omega_1 - \omega_2)$).

Determine the condition on K ensuring the existence of fixed points to the equation for φ . Discuss the nature of the asymptotic regime when this condition is (is not) fulfilled. Qualitatively describe the phase intermittency regime that takes place when the existence condition just misses being fulfilled.

²⁷For a discussion of the physical relevance of this exercise, to be reconsidered in chapter 6, see: O. Dauchot et P.M., "Local versus global concepts in hydrodynamic stability theory," J. Phys. II France **7** (1997) 371–389.

4.6.9 Logistic map (variants)

Consider the map

$$X_{k+1} = f_a(X_k) = a - X_k^2 \quad (4.69)$$

where $a > 0$ is the control parameter. Draw the graph of f_a , find its fixed points and study their stability properties.

In the following, consider the dynamics of a trajectory starting in the neighborhood of $X_*^{(+)} > 0$ for a close to a_0 where the fixed point bifurcates. Setting $a = a_0 + \epsilon$, rewrite the nonlinear map for $X' = X - X_*^{(+)}$ in terms of $\epsilon \ll 1$ at first order in ϵ .

Check that the map for X' has no fixed point in the neighborhood of $X' = 0$ and that the system bifurcates towards a period-2 cycle by studying the iterated map $X'_{n+2} = g_\epsilon(X'_n)$ as ϵ crosses zero. By an expansion to third order in X'_n conveniently simplified thanks to the assumption $\epsilon \ll 1$. Show that the bifurcated cycle is stable for ϵ small enough.

Derive the change of variables that put (4.69) in the equivalent forms $Y_{k+1} = rY_k(1 - Y_k)$ and $Z_{k+1} = 1 - bZ_k^2$.

4.6.10 Delayed logistic map

Consider the map

$$X_{k+1} = rX_k(1 - X_{k-1}). \quad (4.70)$$

Two initial conditions are necessary to start this recurrence which is thus a second-order discrete-time dynamical system. Its non-delayed version is one of the equivalent variants of the logistic map used in the previous exercise.

1) Convert (4.70) into a first-order system by setting $Y_k = X_{k-1}$, compute the Jacobian of the map and determine its inverse when it is possible.

2) Find the fixed points of the map $X_{k+1} = X_k = Y_{k+1} = Y_k$ and study the stability of the non-trivial fixed point $X_* \neq 0$ as a function of $r \in [1, 4]$. In order to do this, find the eigenvalues of the linearized system and their nature—real or complex—as a function of r . Show that the system displays a Hopf bifurcation in the sense of (4.32) for some value of r to be determined.

4.6.11 Arnold's cat

Consider the discrete-time two-dimensional dynamical system $(X, Y) \mapsto (U, V) = \mathcal{S}(X, Y)$ defined on the torus \mathbb{T}^2 , the unit square (modulo 1),

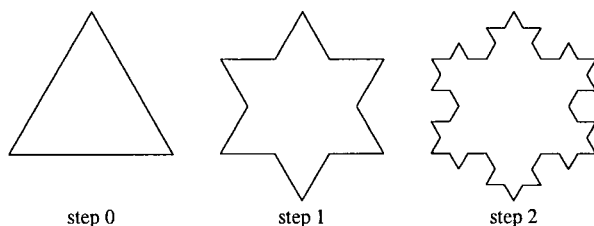


Fig. 4.26 von Koch snow flake.

with opposite sides identified, called “Arnold’s cat map”:

$$U = 2X + Y$$

$$V = X + Y$$

This system is a classical example of chaotic iteration. Determine the inverse map $(U, V) \mapsto (X, Y) = \mathcal{T}(U, V)$ and check that $\mathcal{S} \circ \mathcal{T} = \mathcal{I}$ where \mathcal{I} is the identity map. Compute the determinant of its Jacobian matrix and shows that the system is conservative (Chapter 2, Exercice 2.5.1, p. 61). Illustrate this property by considering the transform of the square $(0, 0), (0, 1/3), (1/3, 0), (1/3, 1/3)$. Show that all trajectories are unstable. Compute the second iterate $\mathcal{S}^2 \equiv \mathcal{S} \circ \mathcal{S}$.

4.6.12 Fractals

Apply formula (4.40) for a topologically connected set, usual line, surface, volume, and observe that it yields its topological dimension as expected. Then compute the fractal dimension of the following objects:

- 1) von Koch snow flake (Fig. 4.26): starting with a triangle with sides of unit length, replace each side by a broken line formed with 4 segments of length $1/3$ as shown in Figure 4.26 and repeat indefinitely the construction on each so obtained segment.
- 2) Sierpinski sets (Fig. 4.27): On the plane, start with the unit square and suppress the central square with side $1/3$; repeat on each of the eight remaining squares; and so on. Same rule but starting with a triangle and dropping the center part. In three-dimensional space, start with a cube cut it into 27 cubes of side $1/3$, suppress seven cubes, the six in the middle of the sides and the center one, repeat indefinitely to get a fractal sponge.
- 3) Cantor dust (Fig. 4.28): Take the square and keep the elements shown,

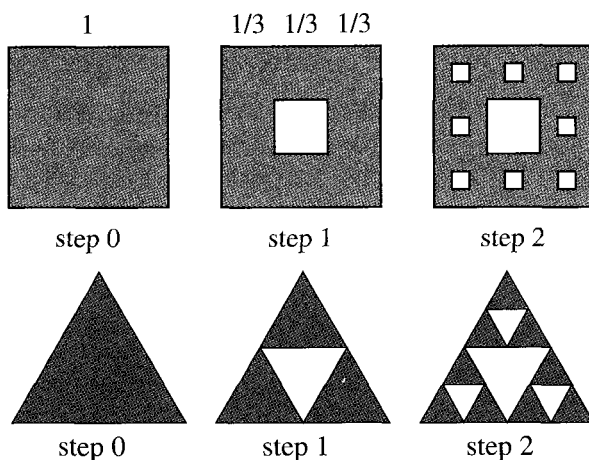


Fig. 4.27 Two-dimensional Sierpinski sets.

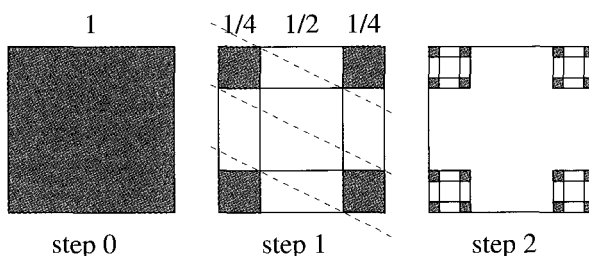


Fig. 4.28 Cantor dust.

repeat indefinitely. Observe that the fractal dimension can be an integer and that here the result could have been obtained by noticing that, at every step, the whole set is in one-to-one correspondence with a continuous interval (by projection along the indicated direction).

4.6.13 Curry–Yorke model (transition $QP \rightarrow \text{chaos}$)

Consider a two-dimensional map²⁸ expressed in terms of the two components (X, Y) components of a complex number $Z = X + iY$, and defined

²⁸J. Curry, J.A. Yorke, “A transition from Hopf bifurcation to chaos: computer experiment with maps on \mathbb{R}^2 ,” Springer Notes in Mathematics **668** (1977) 48ff.

in two steps:

(1) a rotation of $Z_k = X_k + iY_k = |Z|_k \exp(i\varphi_k)$ by an angle φ :

$$\varphi_{k+1/2} = \varphi_k + \bar{\varphi} \pmod{2\pi}$$

and a stretching of the modulus $|Z|_{k+1/2}$:

$$|Z|_{k+1/2} = (1 + \eta) \log(1 + |Z|_k),$$

where η is a control parameter controlling the stability of the fixed point at the origin. (2) a nonlinear transformation is expressed in Cartesian coordinates through:

$$X_{k+1} = X_{k+1/2}, \quad Y_{k+1} = Y_{k+1/2} + X_{k+1/2}^2.$$

The model can be understood as the Poincaré map of a time-continuous system with a limit cycle bifurcating towards a two-periodic regime at $\eta = 0$ and may serve to illustrate the breakdown of a torus into a chaotic attractor.

Draw the attractors obtained numerically for $\bar{\varphi} = 2$ and various values of $\eta > 0$.

[Answer: Fig. 4.29. For $\eta = 0.27$ the attractor is a smooth loop (section of a smooth torus corresponding to a two-periodic regime for the time continuous system). For $\eta = 0.48$, the attractor is a singular curve with fractal structure generated by stretchings and foldings in a regime of developed chaos. These corrugations appear around $\eta = 0.40$ which is thus close to the border of chaos.]

4.6.14 Permanent vs. transient chaos

Consider one-dimensional maps in the form

$$X_{k+1} = \mathcal{F}(X_k)$$

and more particularly the tent map defined by

$$\begin{aligned} 0 \leq X_k \leq 1/2 & \quad X_{k+1} = \alpha X_k, \\ 1/2 \leq X_k \leq 1 & \quad X_{k+1} = \alpha(1 - X_k). \end{aligned}$$

1) Suppose first $\alpha = 2$ and draw the graph of \mathcal{F} and check that interval $\mathbb{I}_0 \equiv [0, 1]$ is invariant in the sense that it contains its image by \mathcal{F} . Then find the fixed points of the map and show that they are unstable. Draw the graph of the iterated map $\mathcal{F} \circ \mathcal{F}$, i.e. $X \mapsto \mathcal{F}(\mathcal{F}(X))$. Find its fixed points and obtain from them a periodic orbit of \mathcal{F} with period 2. Show that this

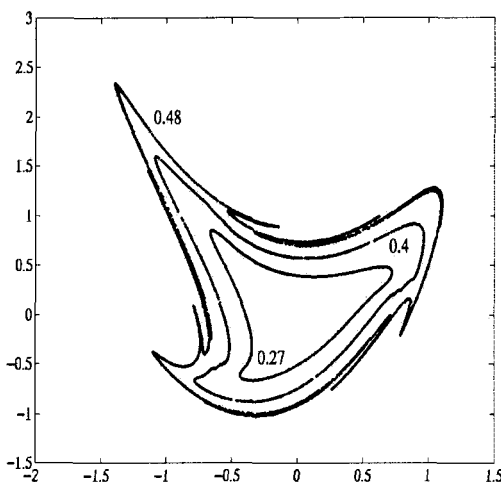


Fig. 4.29 The Curry-Yorke map $\varphi = 2$ and several values of η .

orbit is also unstable. The orbit of an initial condition chosen at random is usually (with probability 1) chaotic. Compute its Lyapunov exponent using (4.37).

2) Suppose now that $1 < \alpha < 2$ and draw the graph of \mathcal{F} . Find the image \mathbb{I}_1 of \mathbb{I}_0 and the image \mathbb{I}_2 of \mathbb{I}_1 , so that the definition interval of the map can be restricted to \mathbb{I}_1 . Show that all trajectories are unstable by computing the Lyapunov exponent.

3) Consider the case $2 < \alpha$. The interval \mathbb{I}_0 is no longer invariant. Draw the corresponding graph of \mathcal{F} and find the set \mathbb{J}_1 of initial conditions that escape at the first iteration. Construct the pre-image \mathbb{J}_2 of this set, *i.e.* such that $\mathcal{F}(\mathbb{J}_2) = \mathbb{J}_1$, to find initial conditions that escape in two iterations, and notice that it is made of two disconnected parts \mathbb{J}_2^1 and \mathbb{J}_2^2 . Continue and observe that the initial conditions that do not escape belong to a Cantor set. When $\alpha = 3$, the construction rule is exactly that of the triadic Cantor set. From the formula, compute the Lyapunov exponent of a trajectory starting right on this set (and remains in it). Such an unstable invariant set is called a *chaotic repeller*.